University of Southampton

Fourier and Wavelet Analysis of Skin Laser Doppler Flowmetry Signals

MPhil Thesis

Wei Qi
CED Group, School of Engineering Sciences [1]

April, 2011

[1]In partial fulfillment of the requirements for the degree of Master of Philosophy.

Abstract

Objective

This thesis examines the measurement of skin microvascular blood flows from Laser Doppler Flowmetry (LDF) signals. Both healthy subjects and those with features of the metabolic syndrome are studied using signal processing techniques such as the Fourier and Wavelet transforms. An aim of this study is to investigate whether change in blood flow at rest can be detected from the spectral content of the processed signals in the different subject groups. Additionally the effect of insulin is examined via hyperinsulinemic euglycemic clamp together with measurements made from a low power 1mW, standard separation (0.5mm) probe and a high power 20mW, wide separation (4mm) probe.

Research design and Methods

We studied a cohort of individuals with 3 or more features (obesity, insulin resistance, etc) of metabolic syndrome (MS) as group 1 ($n = 17$), and also second measurements of the same subjects taken 6 months later as group 2 ($n = 12$ because not every subject in group 1 participated a second measurement). Our study also included 3 healthy people as the healthy group. Skin blood flow was recorded using LDF monitoring device at rest and in response to insulin during hyperinsulinemic euglycemic clamp. We used fast Fourier transform (FFT) and Wavelet transform (WT) based methods to assess skin blood flow and developed models to characterize insulin-induced blood flow changes.

Results

We demonstrated the application of Fourier and Wavelet analysis in analyzing LDF skin blood signals. For group 1 subjects, by using power spectral density (PSD) and average scalogram, we showed changes of blood flow in response to insulin during hyperinsulinemic euglycemic clamp in all five characteristic frequency bands are not statistically significant. Between group 1 and the healthy group, changes in relative spectral power contributions of some frequency components are statistically significant. We constructed a time-evolution model derived from WT scalogram, and this can be used to study the time-evolutionary changes of the endothelial activity in response to insulin. A preliminary analysis of endothelial activities (pre, low, high insulin) in the time-evolution model is attempted using multiple sinusoidal fitting, the dominant amplitude term has an oscillation of 0.005 rad/s with

very small standard deviation, and the less dominant amplitude oscillation has an oscillation of about 0.0127 rad/s. However, we find it difficult to interpret these oscillations physiologically.

Conclusions
FFT (spectral analysis) and WT (scalogram) based methods together with statistics can be adequately used to investigate controls of skin blood flow by detecting the frequency content of LDF signals. Wavelet analysis has the advantage of obtaining better frequency resolution for lower frequency components (e.g., endothelial activity).

In this cohort of individuals with central obesity who are at risks of developing cardiovascular diseases (CVD), our analyses show that insulin-induced vasodilatory effects are impaired.

Acknowledgments

I wish to express my gratitude to my supervisors Dr. Andrew Chipperfield and Prof. Geraldine Clough for their support in the past two years, without which this thesis would not have been possible.

Contents

List of Figures

Chapter 1

Introduction

1.1 Overview

Laser Doppler Flowmetry (LDF) is a non-invasive method for monitoring blood flow in superficial tissues, e.g., skin microcirculation. It has been widely used as a clinical and research tool ever since its introduction in 1975 [52] to explore microvascular perfusion changes under physiological and pathophysiological conditions. One major advantage of LDF is that it is capable of quantifying changes of blood flow in response to stimuli without disturbing the normal state of the subject [52]. These stimuli may include endothelium-related dilator substances, delivered by iontophoresis, arterial occlusion and local heating. It is sensitive and therefore able to capture blood flow changes in response to stimuli [13].

LDF signals are made up of a number of physiological oscillations and when analyzed in the frequency domain, their peaks can be noticed. These oscillations include: 1. Cardiogenic activity (0.4-1.6 Hz) represents the heart beat; 2. Respiratory activity (0.15-0.4 Hz) is the rhythmicity of breath; 3. Myogenic activity (0.06-0.15 Hz) represents rhythmic activity of vessels, 4. Neurogenic activity (0.02-0.06 Hz); 5. Endothelial activity (0.0095-0.02 Hz) corresponds to metabolic activity [51] [50].

Literature suggests that the relative contribution of power spectral density (PSD) of these bands is indicative of vascular (function) health and reactivity. Changes in vascular function are well recognized to be associated with cardiovascular diseases (CVD) such as hypertension, coronary heart disease, peripheral vascular disease and diabetes. There are a number of CVD risk factors that give rise to changes in vascular functions, e.g, obesity, in-

sulin resistance, and aging. Metabolic syndrome is mainly characterized by obesity and insulin resistance. And this will be briefly reviewed in Chapter 2.

This thesis studies changes to blood flow measured by LDF at rest for healthy people and in response to insulin for a cohort of individuals with features of metabolic syndrome by exploring the frequency components of LDF signals using Fourier and Wavelet based methods.

1.2 Chapters

Chapter 2 contains the background literature review relevant to this thesis. Related physiology is briefly described, this is followed by a short review of common assessment methods used in assessing vascular functions. LDF is introduced in more detail which includes measurement and limitations. The relevant and necessary mathematical foundations of Fourier analysis and Wavelet analysis are then briefly summarized. Information on ethics committee approval and softwares used are given at the end of the chapter.

Chapter 3 describes our study population, LDF monitoring device set up (laser probes), and followed by descriptive statistics of the data sets. Fourier analyses of the LDF signals are presented, including PSD. Normality of results is tested before relative spectral power contributions are compared using two-tailed Student t-test. Sensitivity of Fourier transform parameters are also tested, i.e., choice of window function and overlap percentage.

Chapter 4 employs Wavelet transform to analyze LDF signals due to its advantage in having good frequency resolution for lower frequency components. Comparisons have been made with PSD from the average scalogram. Results obtained are in general agreement with Fourier analysis as would be expected.

Chapter 5 attempts to exploit the WT's advantage in resolving lower frequencies, which may suit our study of the endothelial activity band. A time-energy evolution model is presented which gives us a different perspective for analyzing the LDF signal. A sinusoidal fitting scheme of the endothelial band time-evolution curves is also described, changes in oscillatory differences for pre, low and high insulin measurements are presented.

Chapter 6 summarizes this work and presents ideas for further research.

Chapter 2

Background

2.1 Overview

In this chapter, we will review the following background literature:

- A brief introduction of human/skin circulation, insulin-resistant states associated with microvascular dysfunctions.
- Laser Doppler flowmetry.
- Fourier analysis.
- Wavelet analysis.

2.2 Physiology and Methods

2.2.1 Human Circulation

Overview

Cells as individual identities have long evolved into organs or tissues with increasing complexity. To keep this collective system functional and stable, homeostasis must be maintained, therefore an evolutionary necessity of this is the development of a circulatory system to deliver nutrients, transport oxygen, hormones and remove waste products of metabolism [50] to organs and tissues. Circulation also regulates body temperature [33].

The cardiovascular system consists of the heart, blood vessels and blood [47], this can be illustrated in Fig. 2.1. Blood is ejected from left ventricle (systole) and flows through the aorta and then is progressively distributed to

smaller arteries, arterioles and the capillary bed where major regulation of tissue perfusion occurs. Blood returns to the heart via the venous system and eventually fills the right ventricle and atrium from where it will be transported to the pulmonary system (Lung) and oxygenated, after oxygenation blood again enters the left atrium (diastole) and completes a full body circulation. Mechanically, the system maintains a balanced relationship between pressure and resistance [22] through local and systemic controlling mechanisms. Blood flow is proportional to blood pressure and inversely proportional to vascular resistance. However vascular resistance is also modified by biochemical agents through vasodilatory and vasoconstrictive mechanisms.

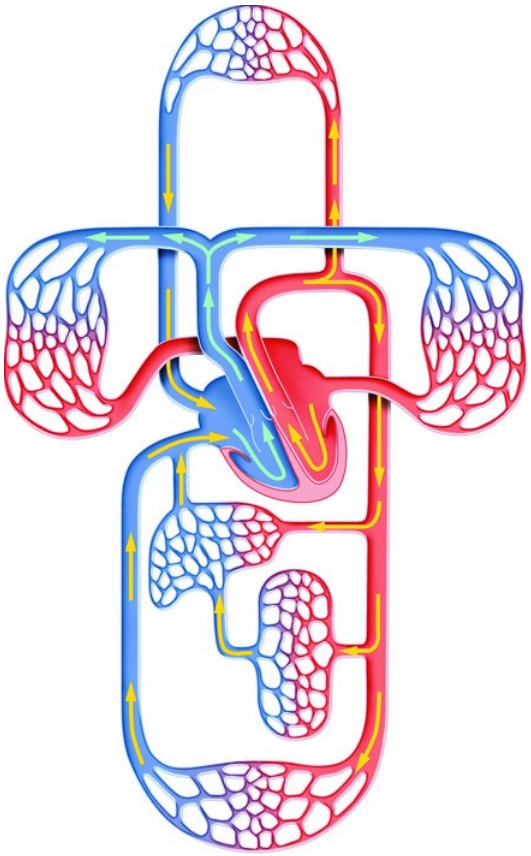

Figure 2.1: Artistic impression of the human circulation. Reproduced from Dorling Kindersley Clip Art

Microcirculation describes blood flow of small vessels (diameter $< 100\mu$m), this is represented as webbed microvascular beds in the above figure. These

vessels include arterioles (mean diameter: 30μm), capillary (8μm) and venules (20μm) [47]. It is the primary site for exchange of materials between interstitial. A typical capillary bed can be illustrated in Fig. 2.2.

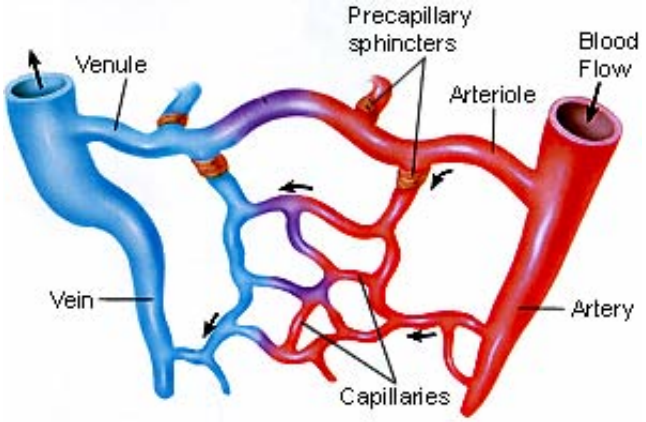

Figure 2.2: Artistic impression of the a capillary bed. Reproduced from Dorling Kindersley Clip Art

There are many types of diseases associated with macro and microcirculation dysfunction, for example, atherosclerosis, hypertension, peripheral vascular disease, coronary disease and diabetes, which is a major risk factor for cardiovascular diseases (CVD) [29] whose microvascular complications include retinopathy, neuropathy, diabetic foot, nephropathy, etc.

Metabolic syndrome (MS) is defined by a cluster of factors that may predispose individuals to cardiovascular diseases (CVD) and type 2 diabetes. Prevalence of metabolic syndrome in the adult population in developed world is suggested to be around 15%-30% [9]. For example, in the U.S. the age-adjusted prevalence is about 23.7% [20].

According to ATP-III (the National Cholesterol Education Program Adult Treatment Panel-III), having 3 or more of the 5 features (central obesity, raised triglycerides, reduced HDL-cholesterol, hypertension, raised fasting plasma glucose) can be classified as MS [9]. These features have been known to be associated with impairment in tissue blood flow, e.g., impaired skin capillary recruitment [45], impairment in endothelium-dependent vasodilation [19], altered functional hyperemia [27] and endothelial dysfunction occur during the early onset of MS [18] and type 2 diabetes [35] which usually

happen before more serious vascular damage.

Insulin resistance is responsible for obesity, hypertension, type 2 diabetes and atherosclerotic CVDs [17]. And insulin resistance is probably the cause of endothelial dysfunction [40]. Features of MS and type 2 diabetes may be called the insulin-resistant states.

Cardiovascular risks may be assessed by examining endothelial function, reactivity and sensitivity of blood flow in response to functional challenges such as post-occlusive hyperemia, local heating, or in response to certain biochemical stimulants, such as insulin, acetylcholine, and sodium nitroprusside.

Skin Blood Flow

The human skin is the largest tissue of the human body, about 16% of total human body weight [47]. It contains multiple layers: the epidermis (around 100μ m) which forms a protective barrier, dermis and hypodermis, as shown in Fig. 2.3. The hypodermis (around 10mm) contains adipose tissue for insulation (thermal and mechanical).

Dermis (around 1.3mm) is a loose connective tissue that contains blood vessels, muscles & etc. This region contains a microvascular network where nutrients and waste products exchange. Circulation at this region is sometimes known as nutritional flow. In human extremities, arteriovenous anastomoses (AVA) exist to regulate temperature. And blood flow through arterioles and venules is the thermoregulation flow [33]. These vessels are under cutaneous sympathetic vasomotor control.

Skin blood flow is sensitive to thermoregulation, and is essential for delivering nutrients, it's part of the microcirculation network, and therefore many local and central mechanisms are present in the skin blood flow, and it is also probably the most accessible site for experiments. Hence skin can be used a surrogate of deeper tissues such as muscle, kidney or tissues and organs which are less accessible. Using a non-invasive technique to continuously monitor skin blood flow may therefore enhance our understanding of the endothelial function as a whole.

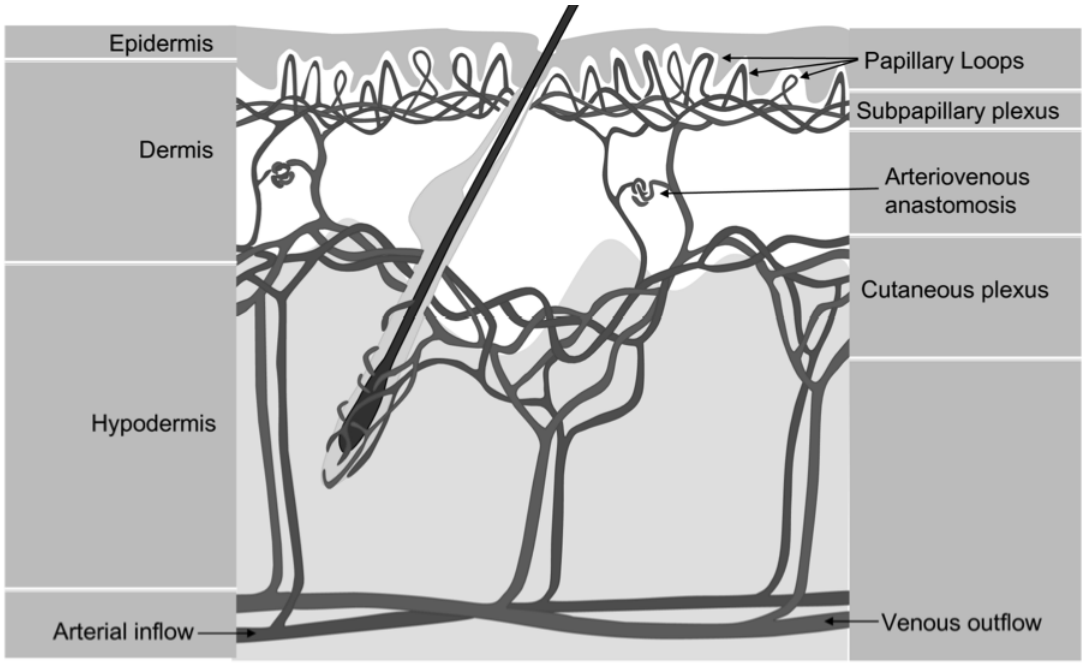

Figure 2.3: Artistic impression of the human skin anatomy. Reproduced from [36].

Endothelial Function

Endothelium is a cell-lining on the lumen and connected to the basal lamina of vessels. [33] A coating of biopolymer on endothelial cells is called the glycocalyx. The glycocalyx and endothelial cells form the endothelium, thus the endothelium plays the central role in regulating vascular homeostasis, its primary role is to retain blood plasma while allowing nutrients to pass through (a semi-permeable membrane). The endothelium releases vasodilator agents such as nitric oxide (NO), initially known as the endothelium-derived relaxing factor (EDRF) [28], endothelium-derived hyperpolarizing factors (EDHF) and prostacyclin in response to sensing the shear stress generated by blood flow [23], as well as in response to acetylcholine [24].

The primary role for NO is the continuous modulation (through vasodilation) of basal tone. Basal tone is the initial (partial) contraction state of resistance vessels [33], this can be illustrated in Fig. 2.4. Shear stress stimulation accounts for approximately 60-80% of NO production while insulin's role is less important, i.e., a less potent dilator during hyperinsulinemia [14].

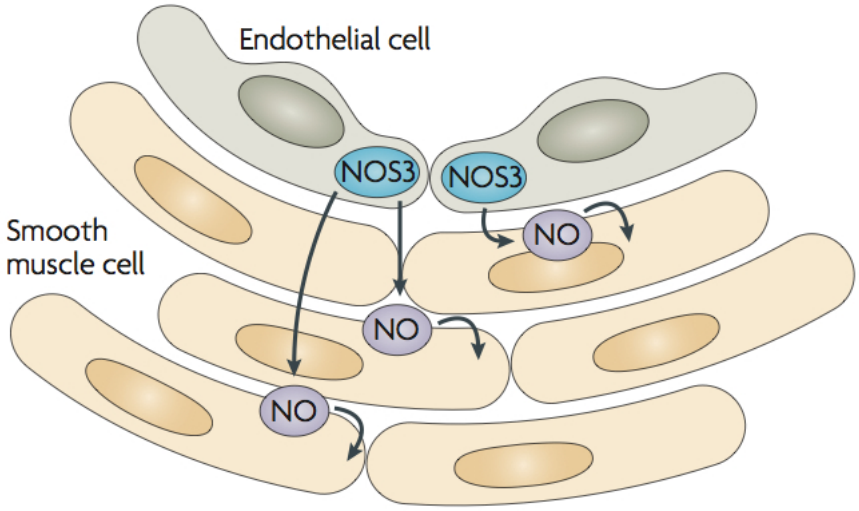

Figure 2.4: A scheme for endothelial cells and the release of NO to relax vascular smooth muscle cells . Reproduced from [41].

The vascular effects of insulin as an endothelium-dependent vasodilator has been studied by various authors [15] and it is known that insulin has a direct action on blood vessels to modulate endothelial activity and vasomotion responses. There is sufficient evidence that insulin is capable of increasing access to insulin itself and muscle cell glucose uptake [15] through capillary recruitment [11].

The endothelium also secretes another vasoconstrictive agent, known as the endothelin (ET-1) [57]. And it is suggested that endothelin may contribute to the basal tone of resistance vessels to a small amount. It is also reported that insulin stimulates both endothelin and NO in human forearms, these two vasoactive agents have opposing effects [10]. ET-1 may be an important component of endothelial dysfunction, as it is found that level of ET-1 is elevated in subjects with insulin resistance [34].

2.3 Assessment Methods

Previously high resolution ultrasound has been used in the assessments of endothelial function of arteries through flow-mediated dilation, such as endothelium-

dependent vasodilator NO or prostacyclin, for example, on the brachial artery, but with poor reproducibility [26]. Other techniques include pulse wave velocity and augmentation index on the brachial artery measured using pulse wave analysis [56].

There are several assessment methods for measuring microvascular functions. For example, the strain-gauge venous plethysmography for studying forearm blood flow, the results are usually reproducible, but this method is invasive (requires brachial artery catheterization) [13].

LDF has been used extensively by researchers to assess endothelial function in both healthy, athletic subjects and those who have vascular diseases [43] [32] [16]. In these studies, experiments were designed specifically to assess various microcirculatory functions, measured at baseline, during occlusion, and post-occlusive reactive hyperaemia (PORH), and also during hyperinsulinemic euglycemic clamp.

Spectral analysis is a common tool for breaking down time series into constituent cycles and is used extensively in engineering disciplines such as electronics and statistics. It has been previously used to analyze human blood flow before and after exercises [32]. Wavelet analysis is a technique that has also been used in analyzing low-frequency oscillations of LDF blood signals [31]. LDF blood flow signals are captured as time series. The ability of LDF to capture oscillations existing in blood flow may be illustrated in Fig. 2.5.

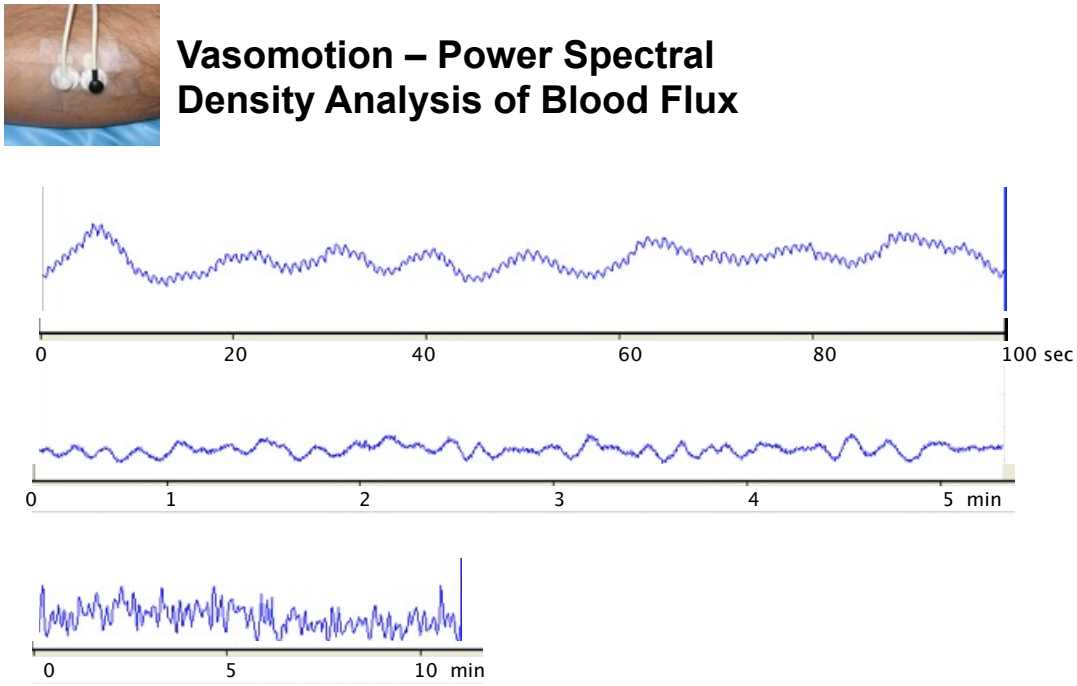

Figure 2.5: LDF measurements zoomed at 100 sec, 5 min and 10 min respectively.

2.3.1 Laser Doppler Flowmetry

The LDF technique takes advantage of the Doppler effect, which is seen as a frequency shift in coherent monochromatic light waves scattered from moving red blood cells (erythrocytes) in the blood [37]. A LDF device uses two laser probes, one is the light-emitting probe and the other is the receiving probe. The emitted light is able to penetrate a certain amount of tissue depth. A scheme is illustrated in Fig. 2.6.

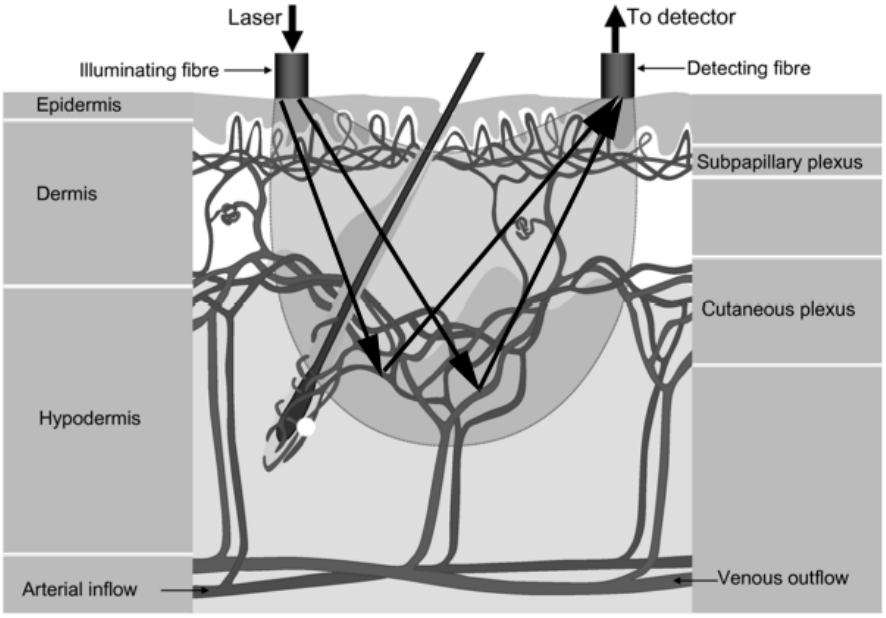

Figure 2.6: LDF measurement scheme. Reproduced from [36].

For our study, we use the DRT4 LDF device (as illustrated in Fig.2.7) manufactured by Moor Instruments Ltd, UK, a 785nm wavelength, high power 20mW, wide separation (4mm) probe (DP1-V2-HP probe, Moor Instruments UK) and a 785nm wavelength, low power 1mW, standard separation (0.5mm) probe (class 3A per BS EN 60825-1:1994) which have been estimated (using Monte Carlo simulation [12]) to peak at approximately 1.7mm and 0.7mm (tissue depth) respectively, signifying that the high power probe can detect significantly more photons, as shown in Fig. 2.8. This indicates that the high power probe may be used in detecting vessels in deeper tissue, i.e., muscles. All our LDF measurements are taken at a sampling rate of 40Hz.

Figure 2.7: LDF device, DRT4, Moor Instruments.

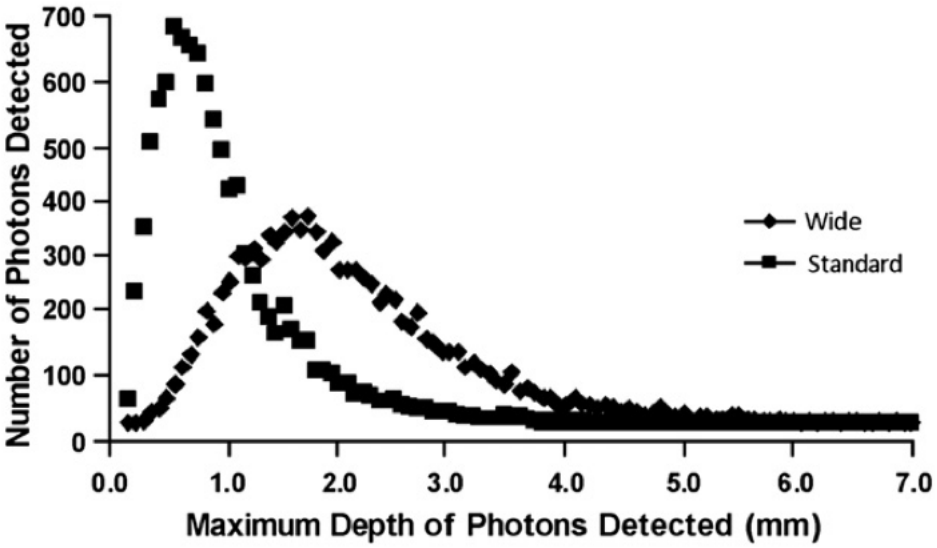

Figure 2.8: Monte Carlo simulation of laser probe detection depth. Reproduced with permission from [12].

2.3.2 Measurement

A typical LDF skin blood signal of baseline is illustrated in Fig. 2.9 which contains measurements of flux, red blood cell concentration, speed and ambient temperature. F1 is measured by high power probe and F2 is measured by standard probe. Flux is related to the product of average speed and concentration of moving red blood cells in the tissue sample volume. This is the parameter most widely reported in laser Doppler publications. Red blood cell concentration gives an indication of the number of moving red blood cells in the tissue sample volume. Speed gives an indication of the average speed of red blood cells moving in the tissue sample volume.

Arbitrary units are used for measuring blood flux, red blood cell concentration and speed.

Our instrument also has the capability to record temperatures, as reflected in the following figure. Varying skin temperature is used as a stimuli for assessing microcirculatory functions.

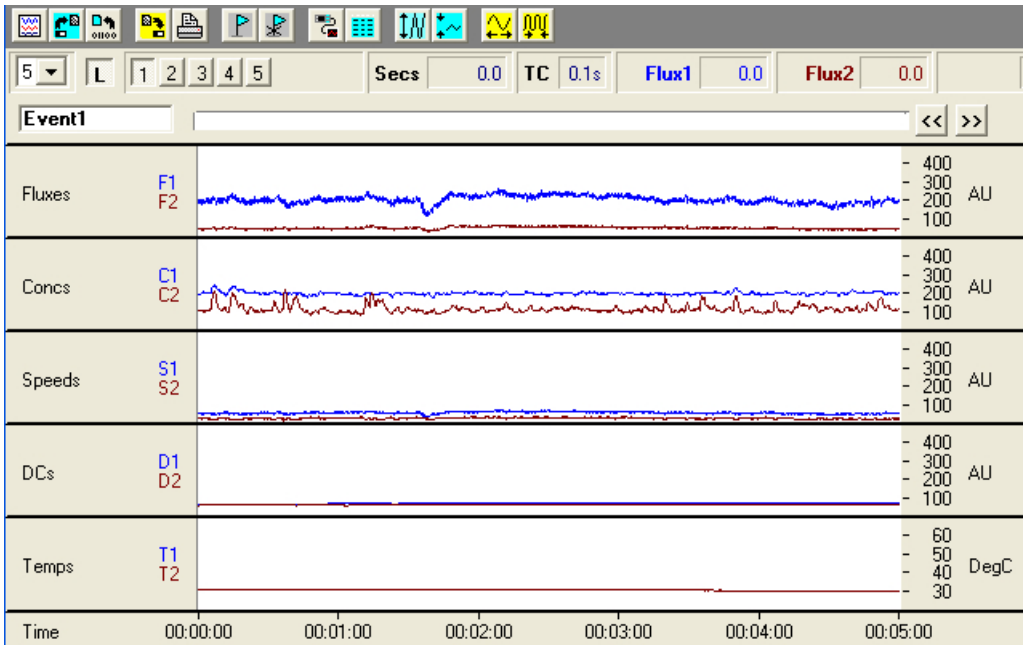

Figure 2.9: LDF signal as displayed on a PC.

All participating subjects fasted and refrained from caffeine containing drinks for at least 2 hours before experiment and acclimatized for 30 min

prior to measurement of blood flow. Experiments were performed in a temperature controlled quiet room (23-24°C). Subject should maintain a supine body position. And our measurements were taken at the calf muscle (tibialis anterior muscle of the lower leg). The whole experimental setup can be illustrated in Fig. 2.10

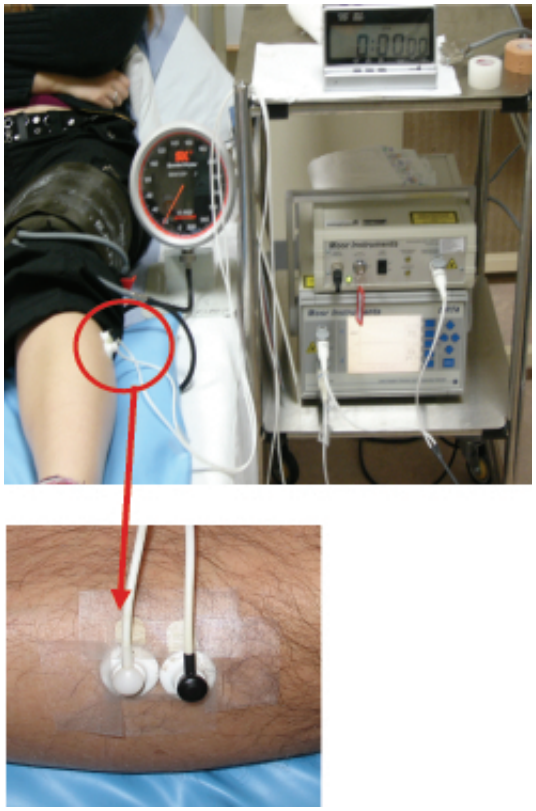

Figure 2.10: Measurement of LDF skin blood flow signal taking place.

2.3.3 Hyperinsulinemic Euglycemic Clamp

The hyperinsulinemic euglycemic clamp was used to measure insulin-mediated glucose disposal rate (M/I). Insulin sensitivity was measured as glucose uptake during infusion of human insulin (Actrapid, Novo Nordisk) initially at a rate of 0.2 mU kg^{-1} min^{-1} for one hour and then at 1.5 mU kg^{-1} min^{-1} for a further 2 hours. All individuals achieved euglycaemia (normal blood glucose concentration) with glucose concentrations clamped at 5.0 mmol/l.

During this 2 h process, we recorded a LDF signal as the pre-insulin measurement before low dose insulin infusion in the last 30 min of low dose insulin infusion, another LDF signal was recorded as the low-insulin measurement, and in the last 30 min at the end of high insulin infusion, a last LDF signal was recorded as the high-dose insulin measurement. This protocol is shown in Fig. 2.11 and was constrained by clinical considerations during this procedure.

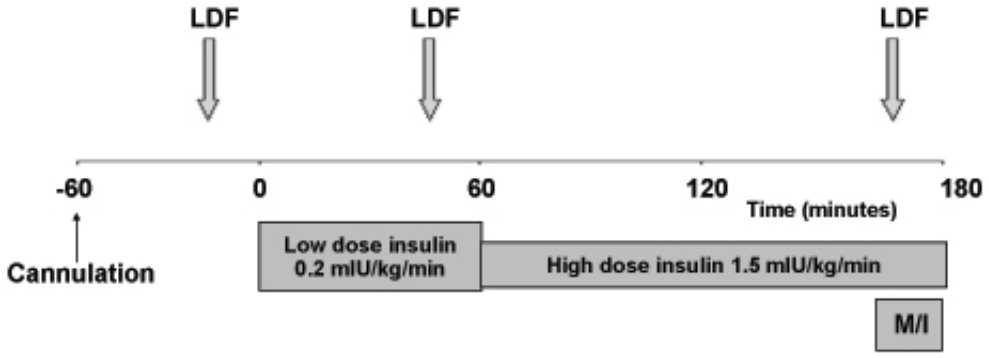

Figure 2.11: A scheme for describing the Hyperinsulinemic Euglycemic Clamp and LDF measurement.

2.3.4 Limitations

Arbitrary Unit

The LDF blood flux uses arbitrary perfusion unit as the exact physical unit (ml/100gm/minute) varies because of the nature of the flow in capillaries and connecting small blood vessels, and the effect of varying skin color and structure, one of LDF's intrinsic limitations.

Movement artifacts

Movement between the probe tip and tissue being measured will cause a Doppler shift and thus produce blood flux artifacts. This can be reduced by fixing the LDF probes with a double-sided sticky ring. Some movement artifacts may be characterized as having the shape of an abrupt spike in the signal. We rejected signals that contain obvious movement artifacts.

Reproducibility

Our data sets were measured from either lower leg or forearm. Even repeated measurements at the same spot (probe location) show temporal variations of up to 25% difference [53]. One study investigated the LDF measurements under identical conditions, on the same site of arm and at the same time of the day, the variation was found to be up to 25.5% [1]. And since microcirculation is subject to multiple factors, we feel that this limitation is difficult to overcome. However, with experiment procedural standardization (i.e., controlled temperature, quiet room) we can minimize the variations.

2.4 Information on Medical Ethics

The study was approved by the Southampton General Hospital Research Ethics Committee (LREC05/Q1704/38) and conducted in accordance with the declaration of Helsinki. All participants were unpaid volunteers and gave informed written consent.

2.5 Software

All Fourier and Wavelet based analyses were performed on MATLAB 2009b (MathWorks Inc). Statistical analysis was performed on SPSS 18.0 (PASW). Other softwares used include Microsoft Excel and LaTeX for preparing this thesis.

2.6 Fourier Analysis

2.6.1 Introduction

The LDF signals we acquired from experiments are represented in time series, i.e., in the time domain. The amount of information we can derive from time domain is rather limited. We require methods which can map signals from time domain to frequency domain to interpret the LDF signals from a different perspective. In the frequency domain we view the signal in terms of the distribution of power spectrum by which the characteristic peaks at certain frequencies can be visualized. Both time and frequency domain methods are complimentary and could provide insights from different perspectives [54].

2.6.2 Fourier Transform

Mathematical Overview

Fourier analysis is based on the mathematical idea of Fourier series, where a time series or continuous function (provided the Dirichlet conditions are satisfied) can be represented as a sum of trigonometric functions. These sinusoidal functions contain frequencies that are harmonics of the fundamental frequency, and thus establish the link between the frequency and time domains.

We begin by reviewing the fundamentals, the evolution and application of Fourier analysis in the biomedical signal processing context from Fourier series to Fourier transform, and from continuous transform to discrete transform respectively.

Fourier Series

The basis functions Fourier chose to represent periodic functions are harmonically related complex sinusoidal functions, written as

$$\exp\left(jn\omega_0 t\right) \tag{2.1}$$

or

$$\exp\left(jn2\pi ft\right) \tag{2.2}$$

where T is the fundamental period and $\omega_0 = 2\pi/T = 2\pi f$ is the fundamental frequency, $n \in \mathbb{N}$. Eq (2.1) refers to the sets of periodic functions with

frequencies that are all multiples of fundamental frequency $2\pi/T$. f is frequency in Hz.

A time series $x(t)$ with period T (i.e., $x(t) = x(t+T)$) can be represented as a linear combination of trigonometric basis functions, or

$$x(t) = \sum_{n\in\mathbb{Z}} c_n \exp(j2\pi fnt), \tag{2.3}$$

where the coefficients c_n's are averaged over the inner product of $x(t)$ and basis functions

$$\begin{aligned} c_n &= \frac{1}{T}\langle x(t), \exp(j2\pi fnt)\rangle & (2.4)\\ &= \frac{1}{T}\int_{-T/2}^{T/2} x(t)\exp(-j2\pi fnt)dt. & (2.5)\end{aligned}$$

Fourier Transform

While the Fourier series is useful for time series trigonometric basis function expansion, the Fourier transform (FT) is essential and necessary when representing the trigonometric series expansion of aperiodic continuous functions, which is the case for most biomedical signals.

For example, the LDF signals are aperiodic, i.e., there is no obvious period associated with them, otherwise the problem of analyzing these signals would become trivial. The Fourier series is an expansion technique for periodic function or series. 15 years after Fourier published his paper that explored Fourier series, he once again found out ways to represent aperiodic functions as weighted integrals of complex sinusoids that are not harmonically related as opposed to Fourier series of periodic functions. For aperiodic functions, we assume that the fundamental period is infinite, or the fundamental frequency (inverse of period) is infinitesimally small. This requires us to resort to integrals in evaluating the Fourier transform of aperiodic signals.

In short, the Fourier transform of an aperiodic continuous function $f(t)$ is expressed

$$X(f) = \int_{-\infty}^{\infty} x(t)e^{-j2\pi fnt}dt. \tag{2.6}$$

and $x(t)$ can be recovered from $X(f)$ as

$$x(t) = \frac{1}{2\pi}\int_{-\infty}^{\infty} X(f)e^{j2\pi fnt}df. \tag{2.7}$$

However, nearly all biomedical signals are analogue signals acquired from electronic devices which need to be sampled at a particular frequency for analysis. The nature of such a sampling process requires us to explore them in discrete time without loss of information.

The Sampling Theorem

For analogue signals to be analyzed with digital computers, they must first be digitized, a process that involves sampling and quantization. Sampling is the process of discretizing the analogue signal with a uniform time interval Δt, (equally spaced) the sampling interval, and the *sampling rate* is the inverse of the sampling interval: $f_s = 1/\Delta t$. It's a proven fact that it's possible to reconstruct a bandwidth-limited signal from equally spaced samples by Whittaker-Shannon interpolation formula [39].

We start from reviewing the Nyquist-Shannon Sampling Theorem, and move on to the discrete representation of Fourier transform.

Mathematically the sampling theorem [38] [46] is stated as follows: Suppose a continuous time signal $x(t)$ is band-limited such that $X(f) = 0$ for $|f| > f_M$. Then $x(t)$ is uniquely determined by its samples $x(nT)$, $n \in \mathbb{N}$ provided the sampling frequency f_s satisfies

$$f_s > 2f_M,$$

where for periodic functions $f_s = 2\pi/T$. This provides a theoretical basis for determining a sampling rate that preserves information content of a signal.

Discrete-time FT

After the sampling process we obtain $x[n]$, a truncated N-point discrete signal with period N. Since the Fourier basis functions are complex sinusoids, the fundamental frequency is simply $2\pi/N$ and k^{th} harmonic is just $\exp(jkn2\pi/N)$. Similar to Eq. (2.4), the discrete-time Fourier conversion for periodic functions can be written as, the coefficients

$$c[k] = \sum_{n=0}^{N-1} x[n] e^{-j\frac{2\pi}{N}kn}. \tag{2.8}$$

Suppose it's sampled from $x(t)$ with a sampling rate of f_s (samples/second). Then the period in seconds is N/f_s, and the fundamental frequency becomes the reciprocal of the this period, i.e. f_s/N Hz. For non-periodic $x[n]$, the period may be assumed to be infinite, i.e., $N \to \infty$ hence the fundamental frequency defined above f_s/N is infinitesimally small, this means the DTFT would be a continuous function in the Fourier domain, or

$$X(\Omega) = \sum_{n \in \mathbb{Z}} x[n] e^{-j\Omega n}, \tag{2.9}$$

where Ω is a multiple of the fundamental frequency.

It's possible now to obtain a reconstruction of $x[n]$ from the DTFT via its inverse transform

$$x[n] = \frac{1}{2\pi} \int_{2\pi} X(\Omega) e^{j\Omega n} d\Omega. \tag{2.10}$$

Here we use Ω for DTFT to distinguish from continuous-time FT which uses ω.

Discrete FT

Again we need to discretise frequencies Ω so as to realize numerical implementation. Based on DTFT (Eq. (2.9)), when we discretize frequencies we obtain the following:

$$X[k\Delta\Omega] = \sum x[n] e^{-j(k\Delta\Omega)n}. \tag{2.11}$$

For numerical implementation, we can only have a finite number of points. Suppose we have N points, and since the Fourier transform $X(\Omega)$ is 2π-periodic, the frequency resolution is therefore $\Delta\Omega = 2\pi/N$. We thus have the Discrete Fourier Transform (DFT) and its inverse:

$$X[k] = \sum_{n=0}^{N-1} x[n] e^{-j\frac{2\pi}{N}kn} \tag{2.12}$$

$$x[n] = \frac{1}{N} \sum_{k=0}^{N-1} X[k] e^{j\frac{2\pi}{N}kn}. \tag{2.13}$$

DFT assumes that the N points of any sampled function $x[n]$ are a single period of $x[n]$, which corresponds to a truncated DTFT of $x[n]$. In any case, the DFT is periodic in the Fourier domain with an interval of $N \cdot (f_s/N) = f_s$ Hz.

Fast Fourier Transform

The Fast Fourier Transform (FFT) is a fast mathematical algorithm [49] that greatly reduces the number of calculations used for obtaining the DFT of a signal. FFT is achieved fastest at a cost of only taking n samples into calculation, where n is a power of 2.

Properties Fourier Transform

When taking the Fourier transform of time signal f multiplied by a window function g, we use the following identity,

$$\mathcal{F}(f \cdot g) = F \star G. \tag{2.14}$$

Eq. 2.14 shows that the FT of a product of a signal and a window function is equivalent to applying the convolution of their respective Fourier transform.

2.6.3 Power Spectral Density

Overview

The FFT can be used to reveal the periodicities contained within the signal, thus it enables us to roughly determine the overall shape and local spectral features. However the frequency resolution of the FFT is fixed across the spectrum and the estimation of power spectral density (PSD) is not usually reliable in analyzing biomedical signals. For example, a direct FFT of LDF signals reveals that the signal energy is clustered mostly around the lower frequency range, but it can hardly give us more details, this will be shown in the next section.

Direct FFT is a classical method for estimating PSD, however it implicitly assumes that data is zero outside the analysis range. This could lead to distortions in the estimate [44]. To improve the reliability of FFT PSD estimation we resort to methods such as average periodogram with overlapping windows, e.g., Welch method [49].

Periodogram

Having reviewed Fourier transform techniques for both continuous and discrete functions, we can apply FT techniques to find out the energy contained within a signal in the frequency domain. Parseval's theorem states that the

Fourier transform preserves the signal's energy in both domains, for an anlog signal $x(t)$, we have

$$\int_{-\infty}^{\infty} |x(t)|^2 = \int_{-\infty}^{\infty} |X(f)|^2 df. \tag{2.15}$$

$|X(f)|^2$ in the right hand side of Eq (2.15) is defined as the power spectral density or power spectrum, or

$$\text{PSD}(f) = |X(f)|^2. \tag{2.16}$$

The periodogram is defined as a direct FFT of a signal followed by averaging,

$$P_{xx}(f) = \frac{1}{N}|X(f)|^2 \tag{2.17}$$

and is therefore a measure of the PSD. The periodogram is equivalent to the Fourier transform of the autocorrelation function [49].

Welch Method

To improve the reliability of PSD estimation by periodogram, one resorts to average periodogram with segments (windowing), or even better, average periodogram with overlapping segments (overlapped windowing), which could statistically improve the estimation. Welch suggested [49] using an overlapping of 50%, which he considers a good compromise.

By default, any truncated data (e.g., taking 600 seconds from LDF blood flux baseline) from a signal for estimating the PSD is multiplied by a rectangular function. The Fourier transform of such a window has slowly decaying sidelobes. In fact the sidelobes decay at a rate of approximately 6dB every octave (where an octave is a change in frequency with a factor of 2 or 1/2) [48]. Such a window may not be an optimal window depending on the type of signals we wish to analyze. For example, in LDF signals, the PSD exhibits clustering at lower frequency range while the high frequency (cardiogenic activity) is noticeable compared with surrounding frequencies and separated at a distance. It is thus beneficial to choose a window with faster decaying sidelobes to prevent the sidelobes from overpowering the cardiogenic activity frequency band. We will have more discussions on this in the Fourier analysis section.

2.7 Wavelet Analysis

2.7.1 Overview

Wavelet analysis from the 1990s has been used extensively in biomedical signal processing and many other fields such as telecommunications, mechanical engineering, etc. It has applications as diverse as detecting engine knocks and oil pipe leakage [42]. In Civil Engineering, Wavelet transform (WT) has been used for system identification [30]. In medical fields, it has been used in analyzing irregular heart rate, turbulent blood flow, hearing aids and other diagnoses [2]. WT can also be used in conjunction with clustering and classification to extract medically useful information [3].

Motivation

Unlike the Fourier transform which transforms time series to the frequency domain only without retaining any time information, the Short-time Fourier transform (STFT) and Wavelet transform simultaneously retain time and frequency information. Like the Fourier transform, the STFT is limited by a fixed time-frequency resolution box, i.e., to resolve high frequency component, the time window needs to be short and vice versa. This poses a disadvantage when analyzing biomedical signals which usually have very dynamic frequency characteristics. For a signal like LDF blood flux that contains multiple frequencies, using STFT, we are forced to choose a frequency resolution that is compromised (not optimal) for all frequencies. Wavelet analysis on the other hand is adaptive in terms of time-frequency resolution.

In other words, we choose the WT over STFT for its ability to be adaptive and a joint time-frequency representation that provides us different perspectives where we can view a signal's time-energy evolution.

Introduction

A fundamental difference of the WT from STFT is the indirect (however, equivalent) manipulation of frequency, i.e., WT treats frequencies as scales. Scale is a concept that is similar to frequency but oppositely defined as we shall see later. WT is achieved by multiplying baby wavelets (generated by a mother wavelet function through dilation) to the original time signal. WT's adaptivity can be interpreted as being able to resolve higher frequency components using small time windows and lower frequency components using

large time windows.

Therefore an intrinsic feature of Wavelet analysis is that it can have very good time resolution for the higher frequency component, and very good frequency resolution for lower frequency components. This is good news for us because LDF skin blood flux signals contain several characteristic lower frequency bands, namely the endothelial and neurogenic bands. And an even lower frequency peak was found to exist in LDF skin blood flux, i.e., which is present in the 0.005-0.0095 Hz band and may involve the endothelium-derived hyperpolarizing factor (EDHF) mechanism [31].

We will primarily use the continuous wavelet transform (CWT) to obtain a time-frequency representation and construct average scalogram from CWT coefficients (which is equivalent to FT coefficients). We use these constructions to perform similar analyses as that will be achieved using FFT. For example, PSD is comparable to the average scalogram.

We emphasize that the Wavelet analysis is not itself superior than the Fourier analysis, but it's not bound by the same fate of FT & STFT (having fixed time-frequency resolution for the entire analysis). WT's time-frequency representation feature is achieved at a cost of having redundant coefficients at each scale (frequency). However the beauty of Wavelet analysis lies in its time-energy evolution perspective. And it also provides us with many interesting applications that cannot be realized by Fourier analysis.

2.7.2 Continuous Wavelet Transform

The notion of the Wavelet transform is to compare the time signal with a series of wavelets generated by the mother wavelet. Mathematically it's defined as an inner product of the signal and the basis function (wavelet), this may be expressed as

$$W(a,b) = \langle f(t), \psi(\frac{t-b}{a})\rangle \tag{2.18}$$

$$= \frac{1}{\sqrt{a}} \int f(t)\psi^* \left(\frac{t-b}{a}\right) dt. \tag{2.19}$$

The scalogram is similarly defined as the spectrogram for STFT

$$\text{Scalogram} = |W(a,b)|^2. \tag{2.20}$$

The inverse CWT can be used to recover $f(t)$, it's expressed as

$$f(t) = \frac{1}{C_\psi} \int \frac{da}{a^2} \int W(a,b) \frac{1}{\sqrt{a}} \psi \left(\frac{t-b}{a} \right) db. \tag{2.21}$$

In Eq.(2.18), a is known as the dilation factor, b is the shifting factor. $\psi(t)$ is the mother wavelet and $\psi((t-b)/a)$ is the translated and dilated baby wavelet. We therefore have for each scale, a fully decomposed transform.

Wavelet Selection

When performing WT, we ask what kind of mother wavelet we should use. The CWT resembles the cross-correlation function, and thus is a measure of similarity between the signal and the wavelet function. The choice of wavelet greatly influences the success of wavelet applications. However, the process of selecting the most appropriate wavelet can hardly be explained by mathematics alone. The best strategy is probably by trial and error [42].

If the wavelet function has good resemblance to the signal of analysis, then we stand a good chance of getting good coefficients [42]. This can best be verified by visual inspection and by trial and error [42].

Previous studies [31] [8] [51] [32] [7] of LDF blood flux by Wavelet analysis have used the complex Morlet wavelet. These authors contend that Morlet wavelet is a good compromise in both time and frequency resolution, i.e., both time and frequency resolution are good. We are forced to make a compromise when choosing a mother wavelet for WT because each individual time-frequency box still cannot escape the fate of Heisenberg Uncertainty principle. This is a similar situation as when we choose Hamming window function for FT.

Morlet Wavelet

The Morlet wavelet in complex form (real Morlet is just a special case of the complex Morlet) is defined to be

$$\psi(t) = \frac{1}{\sqrt{\pi f_b}} e^{i2\pi f_c t} e^{-t^2/f_b} \tag{2.22}$$

$$= \frac{1}{\sqrt{\pi f_b}} [\cos(2\pi f_c t) + i \sin(2\pi f_c t)] e^{-t^2/f_b} \tag{2.23}$$

where f_c is the central frequency in Hz and f_b is the bandwidth parameter. As we can see, Morlet is a Gaussian function modulated by sine waves, as

shown in Fig. 2.12.

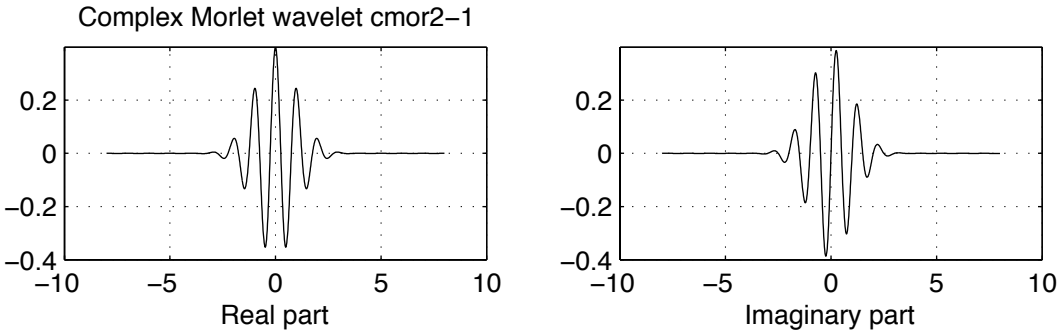

Figure 2.12: Complex morlet wavelet, real and imaginary parts.

The Heisenberg Uncertainty principle states that only Gaussian-like functions can achieve best time-frequency localization [42], this is the motivation behind choosing the complex Morlet wavelet. By Parseval's theorem, Fourier transform preserves energy in both time and frequency domains. The energy of a Morlet wavelet, E, time (t_c) and frequency (ω_c) centres are defined respectively in Eq. 2.24

$$E = \int_{\infty}^{+\infty} (|f(t)|)^2 dt = \frac{1}{2\pi} \int_{-\infty}^{+\infty} (|F(\omega)|)^2 d\omega \tag{2.24}$$

$$t_c = \frac{1}{E} \int_{\infty}^{\infty} t(|f(t)|)^2 dt$$

$$\omega_c = \frac{1}{2\pi E} \int_{-\infty}^{\infty} \omega(|F(\omega)|)^2 d\omega$$

We can also define time (Δt) and frequency (Δ_ω) widths as

$$\Delta_t = \sqrt{\frac{1}{E} \int_{-\infty}^{\infty} (t - t_c)^2 (|f(t)|)^2 dt} \tag{2.25}$$

$$\Delta_\omega = \sqrt{\frac{1}{2\pi E} \int_{-\infty}^{\infty} (\omega - \omega_c)^2 (|F(\omega)|)^2 d\omega}$$

For an ideal localization in time, the wavelet function $f(t)$ should concentrate near the time centre, i.e., a small Δ_t. This is also true for frequency localization. Thus to achieve good localization in both time and frequency domains, the product $\Delta_t \Delta_\omega$ should be small. Next we show that this product

cannot exceed a constant value. Assume our wave function has both time and frequency centres at the origin, i.e., $t_c = 0$, $\omega_c = 0$

$$\Delta_t^2 \Delta_\omega^2 = \frac{1}{2\pi E^2} \int_{-\infty}^{\infty} t^2 |f(t)|^2 dt \int_{-\infty}^{\infty} \omega^2 |F(\omega)|^2 d\omega \tag{2.26}$$

By Cauchy-Schwarz inequality we have the following

$$\int_{-\infty}^{\infty} t^2 f^2(t) dt \int_{-\infty}^{\infty} \left| \frac{df}{dt} \right|^2 dt \geq \left| \int_{-\infty}^{\infty} t f(t) \frac{df}{dt} dt \right|^2 \tag{2.27}$$

since the inequality says for any square integrable functions (finite energy) $f(t)$ and $g(t)$ defined on the interval $[a, b]$, we have

$$\int_a^b |f(t)|^2 dt \int_a^b |g(t)|^2 dt \geq \left| \int_a^b f(t) g(t) dt \right|^2.$$

Observe that the right hand side of Eq 2.27 becomes

$$\int_{-\infty}^{\infty} t f(t) \frac{df}{dt} dt = \int_{-\infty}^{\infty} t \frac{d(f^2/2)}{dt} dt \tag{2.28}$$

$$= t \frac{f^2}{2} \Big|_{-\infty}^{\infty} - \int_{-\infty}^{\infty} \frac{f^2}{2} dt \tag{2.29}$$

$$= -\frac{1}{2} \int_{-\infty}^{\infty} f^2 dt \tag{2.30}$$

$$= -\frac{E}{2} \tag{2.31}$$

using chain rule for differentiation and integration by parts, and since in the above equation

$$t \frac{f^2}{2} \Big|_{-\infty}^{\infty} \tag{2.32}$$

when evaluated in the range of $[-\infty, \infty]$ is 0. Note also that the Fourier transform of df/dt is simply $i\omega F(\omega)$ since by definition

$$\mathcal{F}\left(\frac{df}{dt} \right) = \int_{-\infty}^{\infty} \frac{df}{dt} e^{-i\omega t} dt \tag{2.33}$$

$$= f(t) e^{-i\omega t} \Big|_{-\infty}^{\infty} - \int_{-\infty}^{\infty} f de^{-i\omega t} \tag{2.34}$$

$$= -\int_{-\infty}^{\infty} f(t)(-i\omega) e^{-i\omega t} dt \tag{2.35}$$

$$= i\omega F(\omega) \tag{2.36}$$

With Parseval's theorem, this implies

$$\int_{-\infty}^{\infty} \left|\frac{df}{dt}\right|^2 dt = \frac{1}{2\pi}\int_{-\infty}^{\infty} \omega^2 |F(\omega)|^2 d\omega. \tag{2.37}$$

Now subsitute Eq. 2.37 and Eq. 2.31 into Eq. 2.27

$$\int_{-\infty}^{\infty} t^2 f^2(t) dt \int_{-\infty}^{\infty} \left|\frac{df}{dt}\right|^2 dt \geq \left|\int_{-\infty}^{\infty} t f(t) \frac{df}{dt} dt\right|^2 \tag{2.38}$$

$$\Rightarrow \frac{1}{2\pi}\int_{-\infty}^{\infty} t^2 f^2(t) dt \int_{-\infty}^{\infty} \omega^2 |F(\omega)|^2 d\omega \geq \frac{E^2}{4} \tag{2.39}$$

$$\Rightarrow E^2 \Delta_t^2 \Delta_\omega^2 \geq \frac{E^2}{4} \tag{2.40}$$

$$\Rightarrow \Delta_t^2 \Delta_\omega^2 \geq \frac{1}{4}. \tag{2.41}$$

In other words, the time and frequency resolutions cannot both be arbitrarily small. And in fact the above inequality holds only for Gaussian-like functions, because in order for Eq. 2.27 to hold, the following must hold

$$\frac{d}{dt} f(t) = m \cdot t f(t) \tag{2.42}$$

i.e., df/dt being proportional to $tf(t)$, in which case the ordinary differential equation Eq. 2.42 is solved to be Gaussian-like.

Scale and Frequency

Suppose the transform of a mother wavelet $\psi(t)$ at the origin ($t = 0$), $\hat{\psi}(\omega)$ is concentrated at $\omega = \omega_0$, then for a dilated and translated version of $\psi(t)$ which is $\psi(a^{-1}(t-b))$ has time and frequency centres at $t = b$ and $\omega = \omega_0/a$ respectively. In this way $W(a, b)$, a time-scale representation of signals, also becomes a time-frequency representation function.

To implement continuous wavelet transform, we need to discretize scales. We use the following scheme to discretize scales a. Let a_0 be a constant such that $a = a_0^m$ where m is an integer. And we use the following formula to convert scales to frequencies:

$$f = \frac{f_c}{a \cdot \Delta} \tag{2.43}$$

where Δ is the sampling period (inverse of sampling frequency). For Morlet wavelet, we usually choose f_c to be 1 for convenience (the default central

frequency for real Morlet wavelet is about 0.8 Hz). For example, if we set $a_0 = 1.05$, with f ranging from 0.0095 Hz to 1.6 Hz, we are able to discretize a into 107 scales.

2.8 Summary

In this chapter, we summarized the background literature relevant to this thesis. In physiology, this includes human circulation, especially skin microcirculation, and that microvascular dysfunctions causes changes in vascular functions. And this can be assessed by performing experiments using LDF to measure microcirculation. Skin can be used as a surrogate tissue for this purpose for its accessibility and that it contains both non-nutritive and nutritive flows. LDF experimental setup and equipments are specified, e.g., subject body position, site of measurement, room temperature, etc. The procedure for hyperinsulinemic euglycemic clamp is also included. Information on medical ethics and softwares used are also included.

LDF recordings can be further analyzed using FFT and Wavelet based methods, e.g., to explore LDF signal's frequency content we could use PSD or average scalogram, since it is reported that LDF signals contains at least five characteristic frequency bands, as we have introduced in Chapter 1. These bands represent cardiogenic (0.4-1.6 Hz), respiratory (0.15-0.4 Hz), myogenic (0.06-0.15 Hz), neurogenic (0.02-0.06 Hz) and endothelial (0.0095-0.02) activities. In light of this, the related mathematical foundations of Fourier analysis and Wavelet analysis are also included and discussed.

We briefly proved the uncertainty principle, and showed that time and frequency resolutions cannot both be arbitrarily small, and that Gaussian-like functions can achieve optimal time-frequency resolution.

Chapter 3

Fourier Analysis

3.1 Overview

We have described in the previous chapter the relevant mathematical background for analyzing LDF signals by the traditional Fourier based methods. As such we will look at the signal in the frequency domain, choose an appropriate window and use the Welch method to examine the power spectral density distribution. Based on this method, we will perform the following analyses:

- Estimate PSD for baseline LDF blood flux based on the Welch method.
- Based on estimated PSD, calculate relative energy contribution for each frequency band for signals using high power and standard probes, as well as insulin doses.
- Examine sensitivity to FFT parameters: window, number of overlap.
- Use statistical tests to determine whether changes of blood flow are significant.

The statistics of relative spectral powers are presented in box-whisker plots. Each box is composed of the minimum, lower, upper quartiles, median and maximum values of a sample.

For all statistical tests, we use the two-tailed Student t-test with the null hypothesis that the two samples have equal mean on the 0.05 level of significance. Before these tests, we test normality of samples to ensure they can be used for Student t-test. Test of normality is achieved by using SPSS (Statistical Package for the Social Sciences) 18.

Because our data contain small samples ($n = 17$ or $n = 12$), which is smaller than 30 (the rule of thumb as required by central limit theorem in probability theory [6]), we use the Shapiro-Wilk normal test [55], the null hypothesis is that the data are normally distributed. For p-values smaller than 0.05, the null hypothesis can be rejected. Normality can also be observed on a normal Q-Q plot.

For example, Fig. 3.1 and 3.2 show the Shapiro-Wilk test result and the normal Q-Q plot of the relative spectral power of endothelial activity for 17 subjects measured by high power probe, where p-value is 0.145 and the null hypothesis is not rejected.

Tests of Normality

	Kolmogorov-Smirnov[a]			Shapiro-Wilk		
	Statistic	df	Sig.	Statistic	df	Sig.
VAR00002	.172	17	.195	.920	17	.145

a. Lilliefors Significance Correction

Figure 3.1: Shapiro-Wilk test result.

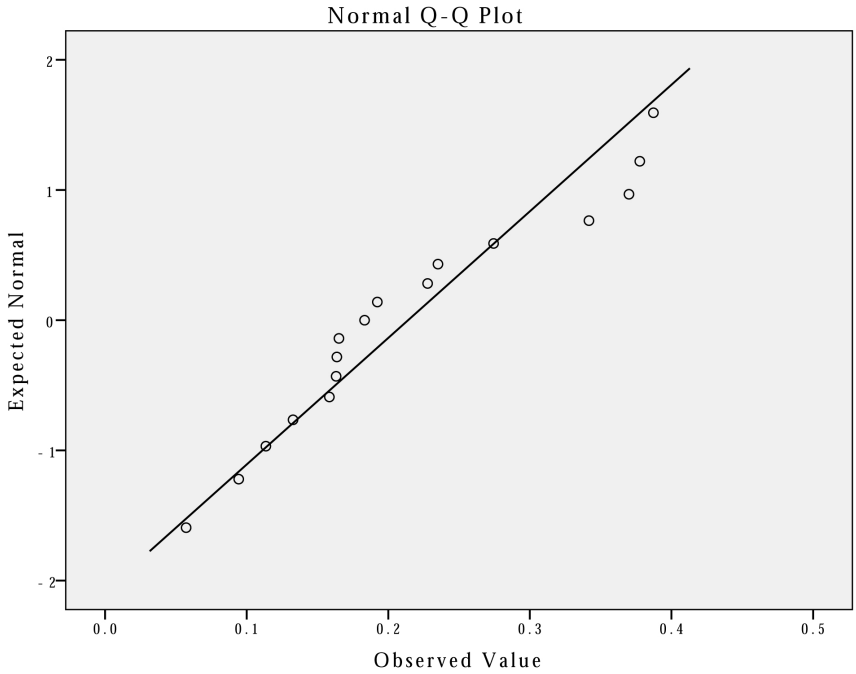

Figure 3.2: Normal Q-Q plot.

3.1.1 Subject Information

For our study, subjects are divided into three groups. The first group (Group 1) contains measurements of 17 subjects, the second group (Group 2) contains measurements of 12 subjects (same subjects as in group 1, but) taken 6 months later, the number is smaller because not everyone in group 1 participated a second visit. There is also a group that contains 3 measurements from healthy subjects (lean mass, non-smoking). These subjects typically have 3 or more features of metabolic syndrome, e.g., obesity (BMI$>$ 30), insulin resistance, etc. Refer to Table 3.1.1 for group 1 subjects information.

Each subject undergoes 3 blood flux measurements, i.e., pre-insulin, low-dose insulin and high-dose insulin during hyperinsulinemic euglycemic clamp as described in Chapter 2.

Mathematically the data are organized as having 2 layers in measurement types and 3 layers in types of insulin dosage challenge or as follows:

Table 3.1: Summary of Participating Subjects

	Group 1 ($\mu \pm \sigma$)
Age (years)	50.40±7.4
BMI (kg/m^2)	30.46±3.89
Mean arterial blood pressure(mmHg)	96.59±8.64

Table 3.2: Data Layers

	Pre-insulin	Low-dose insulin	High-dose insulin
High Power Probe	√	√	√
Standard Probe	√	√	√

Our measurements of the healthy subjects excluded hyperinsulinemic euglycemic clamp test. And due to control of study, detailed information on these measurements will not be stated here, such as age, sex, BMI, mean arterial blood pressure & etc. These three subjects are non-obese (BMI<24) and non-smoking males.

3.2 Analysis of Data

3.2.1 Blood Flux Analysis

Mean, minimum, maximum values and standard deviation are the simplest elements of descriptive statistics. The descriptive statistics of blood flux for group 1 and group 2 LDF signals measured from the high power probe are tabulated in Table 3.3 and 3.4. These data reflect that blood flux (measured by the high power probe) decreases after low-dose insulin infusion and increases again after high-dose insulin infusion, for both group 1 and group 2 subjects.

Statistics for the standard probe measurements are summarized in Table 3.5 and 3.6. For both group 1 and group 2 subjects, we observe slowly increasing blood fluxes after low-dose and high-dose infusions respectively.

The mean blood flux of group 1 and group 2 are illustrated in Fig. 3.3 in the form of box-whisker plots as described in the beginning of this chapter.

Table 3.3: High power probe / Group 1 Statistics (AU)

Baseline	mean	std deviation	min	max
Pre-insulin	81.49	29.03	49.22	172.89
Low dose insulin	76.01	25.67	37.55	129.59
High dose insulin	98.09	36.01	38.05	173.74

Table 3.4: High power probe / Group 2 Statistics (AU)

Baseline	mean	std deviation	min	max
Pre-insulin	84.01	21.45	46.63	111.90
Low dose insulin	75.96	29.65	38.44	143.4
High dose insulin	88.21	32.05	41.55	131.30

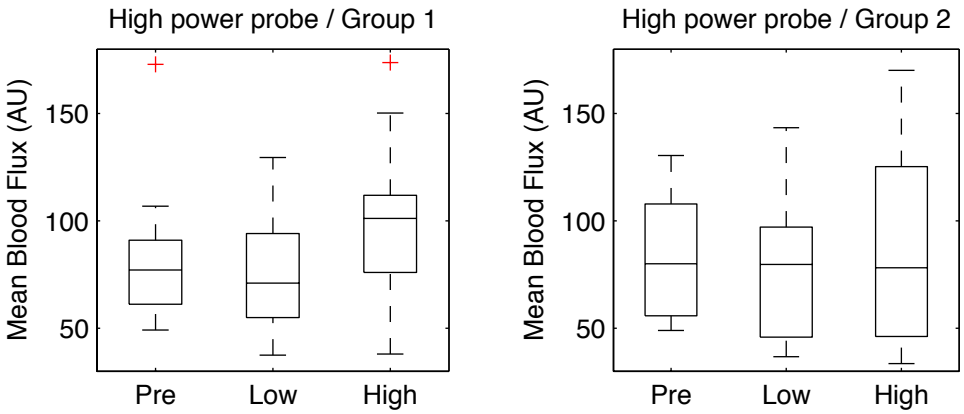

Figure 3.3: Mean blood fluxes for pre, low and high insulin. High power probe/ Group 1&2

Table 3.5: Standard probe / Group 1 Statistics (AU)

Baseline	mean	std deviation	min	max
Pre-insulin	9.35	2.26	5.84	31.96
Low dose insulin	10.29	1.75	6.60	24.62
High dose insulin	11.38	1.74	7.01	21.71

Table 3.6: Standard probe / Group 2 Statistics (AU)

Baseline	mean	std deviation	min	max
Pre-insulin	9.26	1.73	6.18	22.57
Low dose insulin	8.39	1.63	5.46	19.40
High dose insulin	8.52	1.70	5.18	23.99

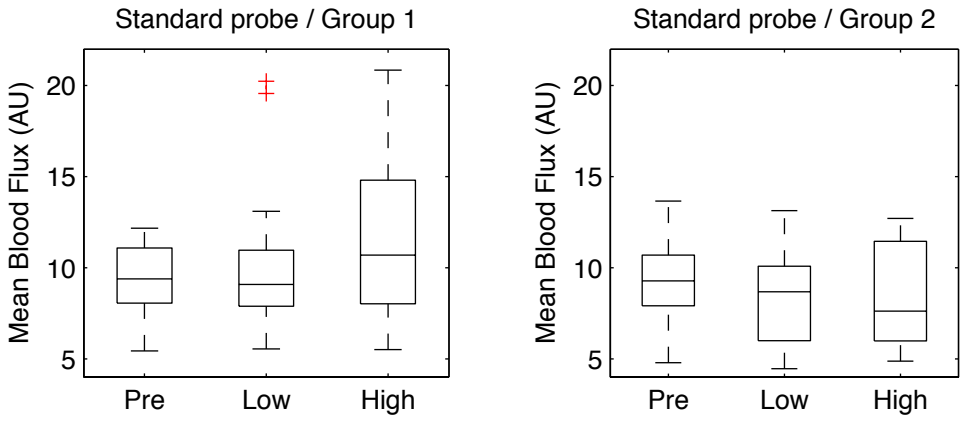

Figure 3.4: Mean blood fluxes for pre, low and high insulin. Standard probe/ Group 1&2

When comparing the mean blood fluxes between group 1 and group 2, we are assessing the changes of microcirculation of these subjects in a course of 6 months. Presumably, if the subjects have altered their diets and exercised more often, we may be able to detect some differences. However, we did not record the weight, BMI, etc of these subjects during their second visit (group 2). We therefore cannot make further conclusions. The $p-$values for comparing changes between group 1 and group 2 mean blood fluxes are

greater than 0.05 (smallest $p = 0.0547$), i.e., there is no statistically significant change of blood flux in response to insulin in a course of 6 months time.

For the high power probe, low-dose insulin decreases mean blood flux (as compared with pre-insulin), high-dose insulin only slightly increases mean blood flux for both groups. For the standard probe, there are small increases for low-dose and high-dose insulin for group 1, for group 2, low-dose and high-dose insulin decrease mean blood flux.

3.2.2 Pre-processing

Before we perform Fourier analysis on the data sets, we need to perform a few pre-processing procedures. We first take one segment of 600 usable seconds from flux baseline before occlusion. This segment is then re-sampled at 10Hz (the original signals have sampling rate of 40Hz) (to get greater resolution over the frequency band of interest) using a low-pass finite impulse response (FIR) filter. A moving average filter of 200s is then applied to remove slow-moving trend. A span of 200s is equivalent to a moving trend of 0.005Hz [12] [5]. The mean is then removed. These procedures attempt to reduce spectral leakage and subsequent PSD estimate bias for the very slow oscillations, i.e., endothelial band (0.0095Hz-0.02Hz).

3.2.3 Power Spectral Density

Power spectrum can be estimated the autocorrelation function. However, we find that estimation of PSD by Fourier transform is more interesting as it gives us more flexibility in controlling parameters (window function, overlapping).

We choose the Hamming window and by default specify a segment length of 200s (one periodogram) with 50% overlapping. 200s is sufficient to contain at least 1 cycle (actual: 1.9 cycles) of the lowest frequency 0.0095 Hz. Hence a total of 5 segments are generated for averaging the periodogram for a signal of 600s. PSD estimation is achieved by the Welch method. Average power is integrated for each of the five characteristic frequency bands. A typical estimation of PSD is illustrated in Figure 3.5.

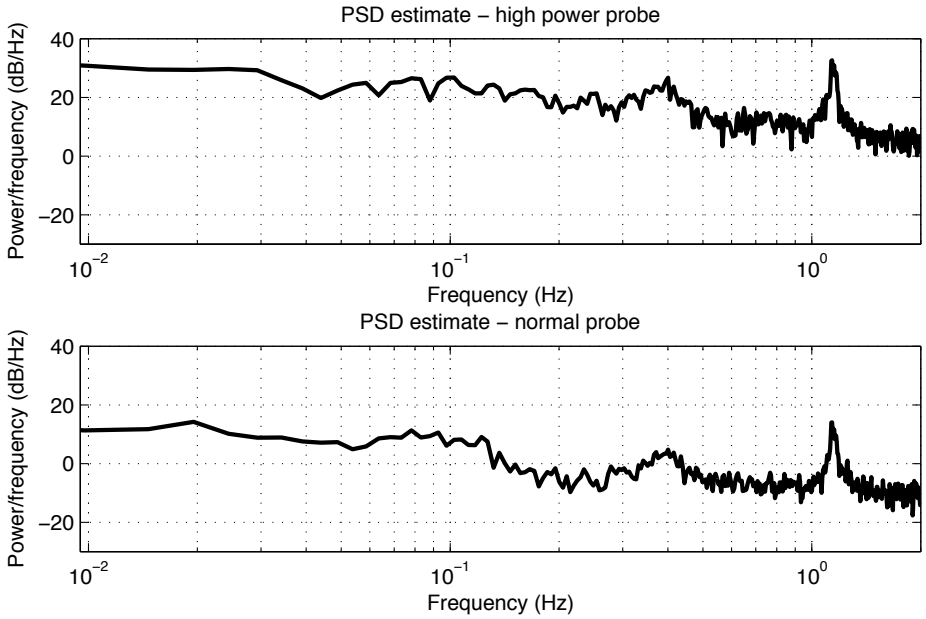

Figure 3.5: An example PSD estimation of signals measured from high power and standard power probes.

3.2.4 Relative Spectral Power

Since individual LDF blood flux varies with amplitude, it's not wise to directly compare flux or spectral amplitude. We use a percentage based quantity to make comparisons. After the PSD is constructed, we calculate relative spectral power contribution of each of the 5 frequency bands using the trapezoidal numerical integration function in MATLAB to integrate the PSD. We will display our results in the next section.

3.2.5 Comparisons

Having looked at Table 3.2, we realize that there are many combinations for cross comparisons. However, typically we would compare differences between:

- High power and standard probes;
- Insulin challenge dosages (pre, low and high).
- A cohort of individuals characterized with metabolic syndrome features (Group 1) and healthy subjects (Healthy Group).

The numbers on x-axis on subsequent box-plots represent the five characteristic frequency bands (in order to save space on plots) and they are explained as follows:

- 1 is for the endothelial band (0.0095 - 0.02 Hz),
- 2 is for the neurogenic band (0.02 - 0.06 Hz),
- 3 is for the myogenic band (0.06 - 0.15 Hz),
- 4 is for the respiratory band (0.15 - 0.4 Hz),
- 5 is for the cardiogenic band (0.4 - 1.6 Hz).

Fig. 3.6, 3.7 and 3.8 show the relative spectral power of pre, low and high insulin dosages respectively for Group 1 (high power and standard probes).

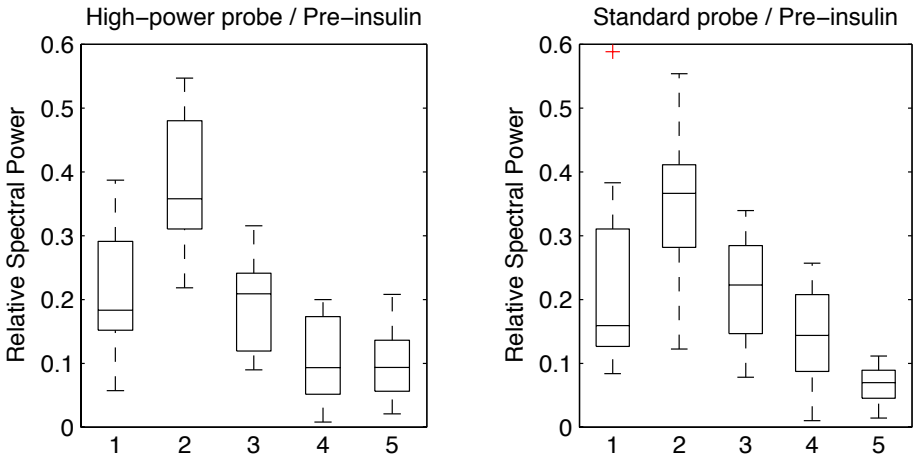

Figure 3.6: Relative spectral power: **pre-insulin**, high power and standard probes.

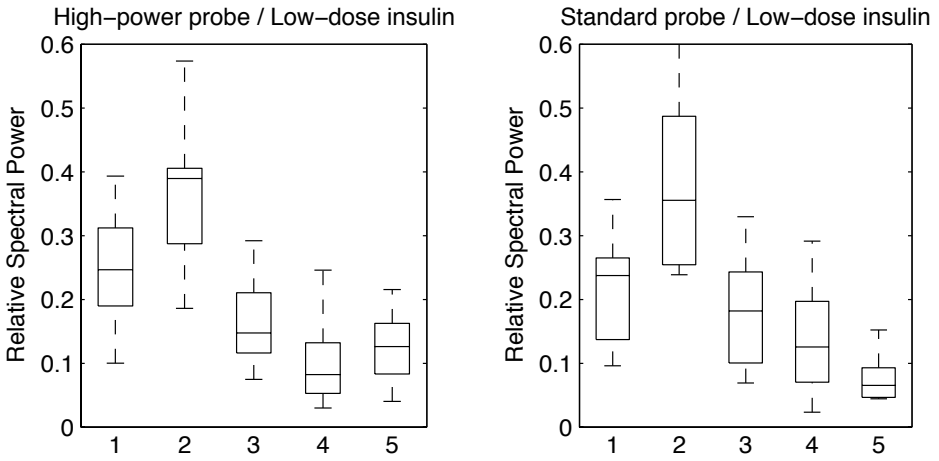

Figure 3.7: Relative spectral power: **low-dose insulin**, high power and standard probes.

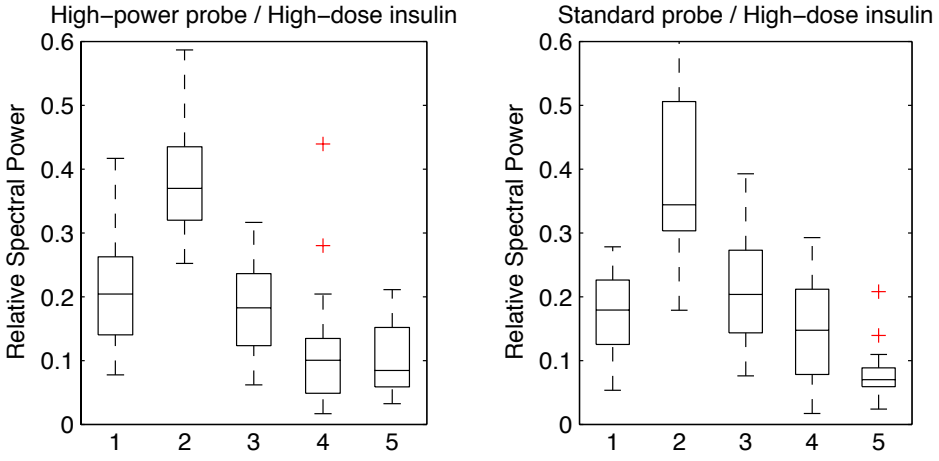

Figure 3.8: Relative spectral power: **high-dose insulin**, high power and standard probes.

Probe differences

It has been reported [12] that for skin LDF signals of non-obese subjects (with BMI<24) the majority of the signal comes from deeper tissue for the

high power probe measurement, while the majority of signals comes from superficial tissue for the standard probe. Deeper tissues are predominantly vasculature in the sub-dermal layer. And this is also confirmed by Monte Carlo simulation in one study [12]. Also in the literature, for the high power probe, relative spectral power of cardiogenic activity contributes significantly more than other frequency bands, and for the standard probe, the endothelial, neurogenic and myogenic activities contribute more than the cardiogenic activity. This applies to the healthy cohort in our study.

However for our cohort of individuals with metabolic syndrome features, cardiogenic activity did not contribute a significant portion of the signal measured by the high power probe, it is weaker than most other activities. This can be viewed in Fig. 3.6, 3.7 and 3.8.

Insulin challenge dosages

We summarize in Table 3.7 and 3.8 the mean relative spectral power from wide and standard probes for group 1 and 2 (29 subjects) and 3 healthy subjects in percentage respectively.

Table 3.7: Mean Relative Spectral Power from **high power probe**. G1/G2 & Healthy, value in percentage (%).

	Endothelial	Neurogenic	Myogenic	Respiratory	Cardiogenic
pre	21.40/30.01	38.33/39.70	19.83/17.36	10.28/6.19	10.16/6.75
low	24.50/30.97	36.19/42.27	16.53/14.13	10.61/5.61	12.17/7.02
high	21.13/24.69	38.35/44.54	17.93/13.95	12.11/6.04	10.48/10.77
healthy	9.35	18.8	16.09	13.02	41.23

For group 1 and group 2 individuals, a slight increase in endothelial activity is observed after low-dose insulin infusion, from 21.40% to 24.50%, and this effect is not observed after high-dose insulin. For neurogenic activity, the contrary is observed, i.e., there is a decrease of neurogenic activity after low-dose insulin. Myogenic activity decreases after insulin infusions. Respiratory activity slightly increases after low-dose and high-dose insulin. Low-dose insulin has a greater effect on cardiogenic activity than high-dose

insulin.

Table 3.8: Mean Relative Spectral Power from **standard probe**. G1/G2 & Healthy, value in percentage (%).

	Endothelial	Neurogenic	Myogenic	Respiratory	Cardiogenic
pre	22.06/25.79	35.72/38.13	21.64/20.39	13.96/10.24	6.62/5.45
low	22.03/28.89	38.4/38.84	18.12/17.34	13.85/9.84	7.61/5.09
high	17.87/23.71	39.11/38.37	20.81/18.89	14.21/12.77	8.00/6.75
healthy	8.54	23.51	18.53	6.44	41.48

A weaker contribution from cardiogenic activity is observed from standard probe, as compared with that from a high power probe. Accordingly, we observe slightly stronger myogenic and respiratory activities.

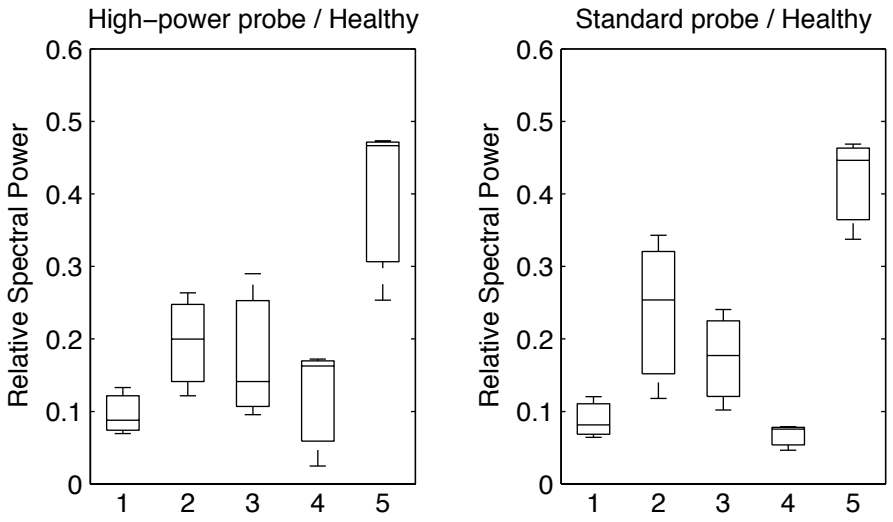

Figure 3.9: Relative spectral power: healthy subjects, muscle and skin probes.

For healthy subjects, we observe a stronger spectral power contribution from cardiogenic activity (high power probe: 41.23% and standard probe: 41.48%), a slight increase in power from the neurogenic activity (high power

probe: 18.8% and standard probe: 23.51%). The respiratory activity (6.44%) from the standard probe is much lower than the value obtained from the high power probe (13.02%).

We calculated p-values (using two-tailed Student t-test) to test whether the changes in relative spectral power in the above mentioned frequency bands are statistically significant, in other words, we want to find out whether differences in mean are induced by chance alone or they have physiological origins. The p-values for comparing relative power spectra between Group 1 and the Healthy group are also presented, to show if there are any differences between the two groups.

Table 3.9: p-values for comparing pre, low, high insulin dosages, high power probe, G1.

	Endothelial	Neurogenic	Myogenic	Respiratory	Cardiogenic
pre vs. low	0.2257	0.7305	0.3179	0.8904	0.2025
pre vs. high	0.8904	0.8095	0.5353	0.9177	0.8633
low vs. high	0.2704	0.7305	0.5128	0.9725	0.2150

Table 3.10: p-values for comparing pre, low, high insulin dosages, standard probe, G1.

	Endothelial	Neurogenic	Myogenic	Respiratory	Cardiogenic
pre vs. low	0.6794	0.9725	0.2416	0.9177	0.6297
pre vs. high	0.6543	0.5353	0.6297	1	0.5728
low vs. high	0.1296	0.9451	0.4282	0.8363	0.7566

Table 3.11: p-values for comparing G1 pre-insulin and Healthy measurements, high power probe.

	Endothelial	Neurogenic	Myogenic	Respiratory	Cardiogenic
G1 pre vs. H	0.0343	0.0149	0.5966	0.5966	0.0081

From Table 3.9 and 3.10, we are able to tell that for group 1 data, the change from low to high-dose insulin is most notable in endothelial activity frequency band ($p = 0.1296$, the smallest p-value, although not in the 95% confidence interval), this is supported by data in Table 3.7 where mean values drop from low to high insulin measurements, i.e., from 22.03 to 17.87. Other notable changes include endothelial activities from pre to low, and low to high insulin, cardiogenic activities from pre to low and low to high insulin.

Table 3.12: p-values for comparing G1 pre-insulin and Healthy measurements, standard probe.

	Endothelial	Neurogenic	Myogenic	Respiratory	Cardiogenic
G1 pre vs. H	0.0263	0.0903	0.4587	0.1123	0.0081

We also obtained p-values for comparing pre-insulin measurement from group 1 subjects with measurements from the healthy subjects. The purpose of this test is to compare the differences in relative spectral powers between healthy and a cohort of individuals with features of metabolic syndrome. The endothelial and cardiogenic activities are vastly different between these two groups in both probes. p-values for these frequency bands are < 0.05. For the neurogenic band, $p < 0.05$ in the high power probe measurement but not in the standard probe measurement ($p = 0.0903$). The myogenic and respiratory activities are less different (i.e., difference is not significant). This possibly reflects that the endothelial, nervous and cardiovascular functions may be impaired or altered in people with metabolic syndrome.

3.3 Sensitivity to FFT Parameters

PSD estimation via FFT is dependent on a several parameters, namely, choice of window, window size and overlap percentage. Although we have the theoretical and empirical knowledge of different shapes and their respective Fourier transforms, it is usually through trial and error that we find the optimal parameters that best suit our analysis.

3.3.1 Choice of Window

The window function's primary role in Fourier analysis is to reduce spectral leakage. Spectral leakage occurs when we perform DFT, and because sidelobes of the FT of window function are separated by null points where frequencies are not calculated due to the finite length of DFT. One way to reduce spectral leakage is through the use of a window function with better frequency response.

As we have mentioned before, truncating a signal to obtain a segment of data for analysis is equivalent to applying a rectangular window to the signal. In other words, an absence of window function is by default a rectangular window. The resulting periodogram may not be optimal due to the frequency characteristics of the rectangular window, a normalized frequency response of this window function is illustrated in Figure 3.10, i.e., the distance between the partial mainlobe and the first sidelobe peak is about 13 dB [4] and subsequent peaks attenuate slowly. As we mentioned earlier, the sidelobes decay at a rate of 6dB per octave. In time domain, an abrupt ending can be observed at the two ends of the window function.

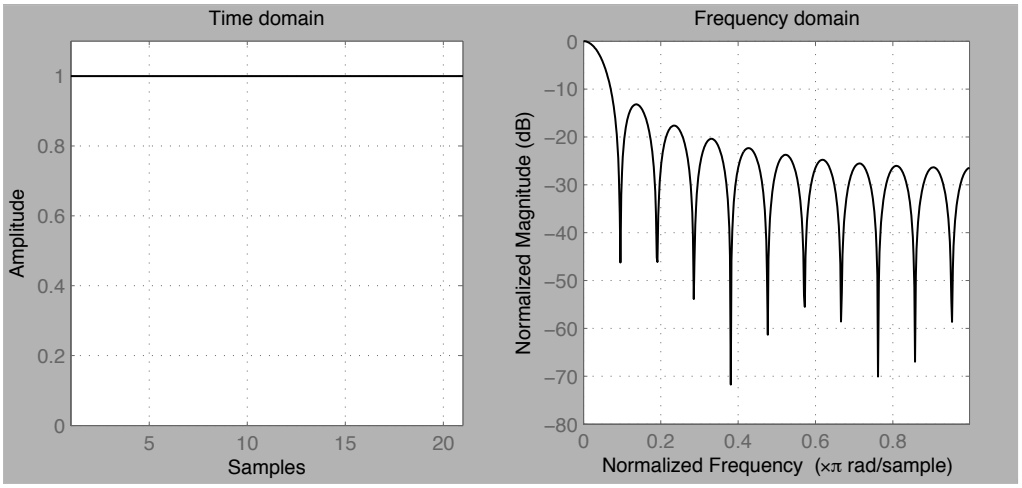

Figure 3.10: Rectangular window (left) time function and its frequency characteristics.

The general feature of our LDF signal can be roughly estimated from a direct FFT, as shown in Figure 3.11. Within the range of 0.0095 Hz to 1.6 Hz, we see two groups of clustered frequencies at around 0-0.15 Hz and 1.2 Hz covering the endothelial, neurogenic, myogenic and cardiogenic activities. These two groups separate at a distance. For a signal with such a frequency characteristic, it may be best to choose a window with moderately decaying sidelobes, so as not to weaken too much the higher frequency part of the signal spectra, since we still have a higher frequency component located at some distance apart.

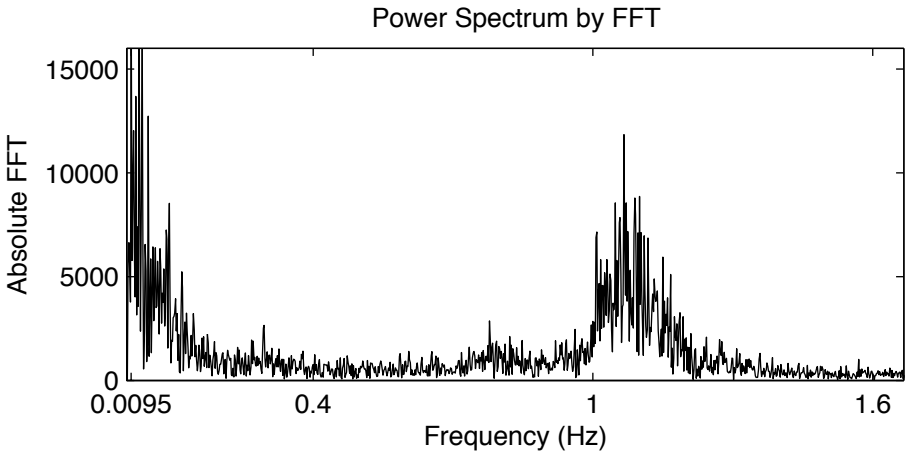

Figure 3.11: Power spectrum by direct FFT shows the general frequency characteristics of a typical LDF signal.

Therefore for LDF signals, we have to make a compromise in choosing the window function. The default rectangular window has sidelobes that decay too slowly, which will strengthen some frequencies with weak amplitudes. Another extreme is to choose a window that has rapidly decaying sidelobes. These extreme windows may include Blackman Harris as illustrated in Fig. 3.12, where a level difference of about 90 dB from mainlobe (compared with 13 dB for rectangular window).

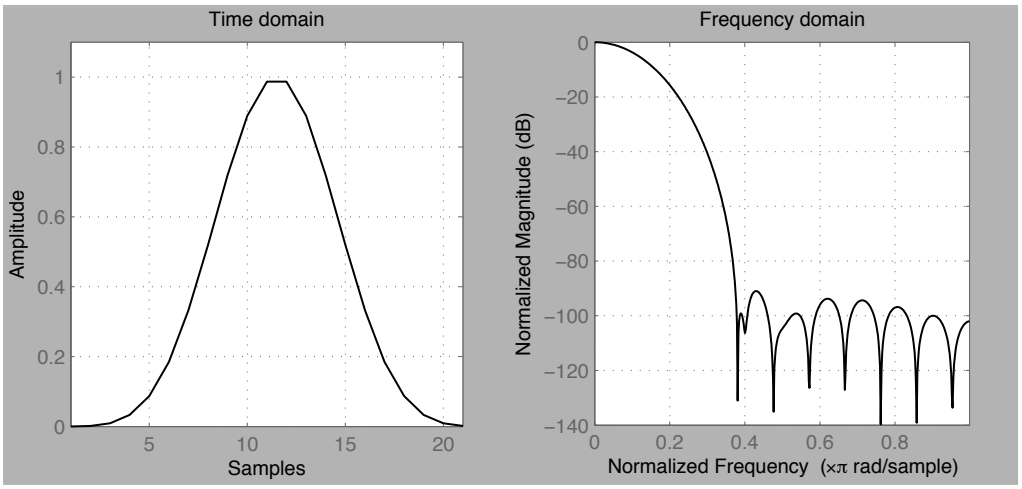

Figure 3.12: Blackman Harris window (left) time function and its frequency characteristics.

The Hamming window on the other hand has moderately decaying sidelobes, which can be illustrated in Fig. 3.13. The first sidelobe has a level difference of about 40 dB from mainlobe (which is in between the rectangular and the Blackman Harris window).

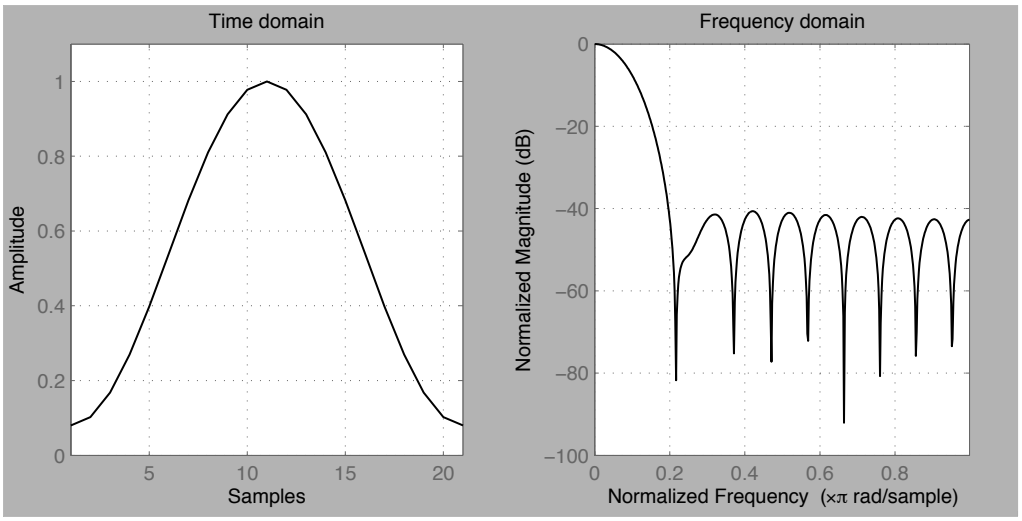

Figure 3.13:) time function and its frequency characteristics.

Properties for the three chosen window functions can be summarised in the following table.

Table 3.13: Properties for rectangular, Hamming, and Blackman Harris windows.

	Leakage Factor	RSA*	Mainlobe Width (-3dB)
rect	9.25%	-13.2dB	0.078
hamm	0.04%	-40.6dB	0.125
blackman	0%	-91dB	0.180

Where RSA* stands for Relative Sidelobe Attentuation, and is the distance between mainlobe peak to the first sidelobe peak. These properties are calculated from MATLAB (Matrix Laboratory, a versatile program for numerical manipulation).

3.3.2 Overlap Percentage

The Welch method assumes a 50% overlap between consecutive windows. As long as the overlap is smaller than 100% and greater than 0%, it is mathematically feasible for performing calculations, however, the resulting periodogram may be different. We only know that going to the extremes may be bad for the analysis, e.g., 99% or 1% overlap. Hence we will perform tests with different window functions and overlapping at 25%, 50% and 75% respectively and observe the differences.

3.3.3 Results

We calculated the averaged relative spectral power using three different window functions and overlapping percentages for the high power probe signals of Group 1 and Healthy group. The results are presented in Fig. 3.14 and 3.15. A table of summary is presented, where p-values are also calculated to test whether the differences of relative spectral power resulted from different window functions and overlapping percentages are significant.

Notice that for both Group 1 and Healthy group, both Blackman Harris and Hamming windows weaken the endothelial activity frequency band (a narrowing of average spectrum) and strengthen slightly the neurogenic and cardiogenic activity bands. This shows that window functions indeed have influence on the power spectral density estimation, although changes are very small in some cases. Notice also that for the rectangular window, there is almost no change in relative spectral power across all five frequency bands, when using different overlapping percentages, since it's unity everywhere in the support (the defined region).

From the results, we first test whether different overlapping percentages using the same window function produce statistically significant difference in relative spectral power across different frequency bands. We use the two-tailed Student t-test to test whether the probability (p-value) that the pair of two samples come from the same distribution, in other words, we want to determine whether the difference is induced by chance.

Table 3.14: p-value for different overlaps, **Blackman Harris**, Group 1, high power probe.

	Endothelial	Neurogenic	Myogenic	Respiratory	Cardiogenic
25% vs. 50%	0.4084	0.9451	0.8363	0.7829	0.9725
25% vs. 75%	0.5582	0.8633	0.9725	0.8633	1
50% vs. 75%	0.8633	0.8363	0.6054	1	0.8904

Table 3.15: p-value for different overlaps, **Hamming**, Group 1, high power probe.

	Endothelial	Neurogenic	Myogenic	Respiratory	Cardiogenic
25% vs. 50%	0.5582	0.8633	0.8633	0.9177	0.9725
25% vs. 75%	0.7048	0.9451	0.7048	0.9177	0.9725
50% vs. 75%	1	0.8633	0.7566	0.8904	0.9725

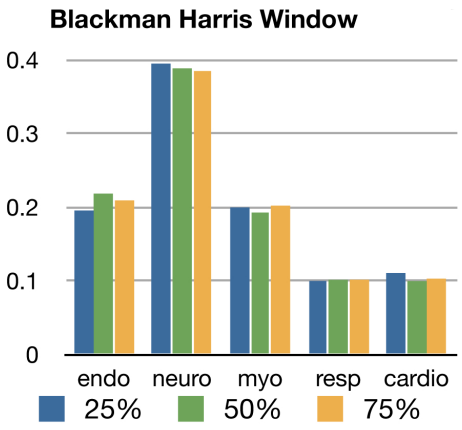

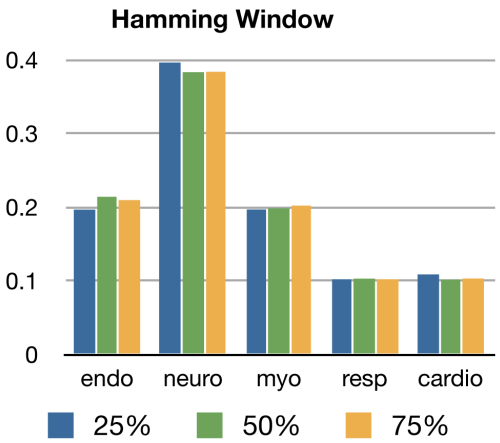

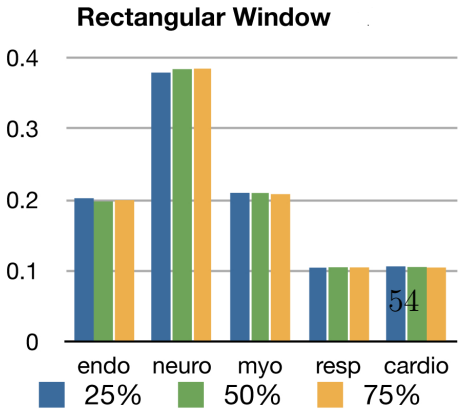

BH	endo	neuro	myo	resp	cardio
25%	0.1954	0.3949	0.1996	0.0997	0.1104
50%	0.2182	0.3884	0.1926	0.1012	0.0995
75%	0.2091	0.3847	0.202	0.1015	0.1028

H	endo	neuro	myo	resp	cardio
25%	0.1966	0.3962	0.1967	0.102	0.1085
50%	0.214	0.3833	0.1983	0.1028	0.1016
75%	0.2095	0.3837	0.2019	0.1019	0.103

R	endo	neuro	myo	resp	cardio
25%	0.2018	0.3789	0.2094	0.1041	0.1058
50%	0.1973	0.3838	0.2093	0.1046	0.1049
75%	0.1991	0.3846	0.2076	0.1044	0.1042

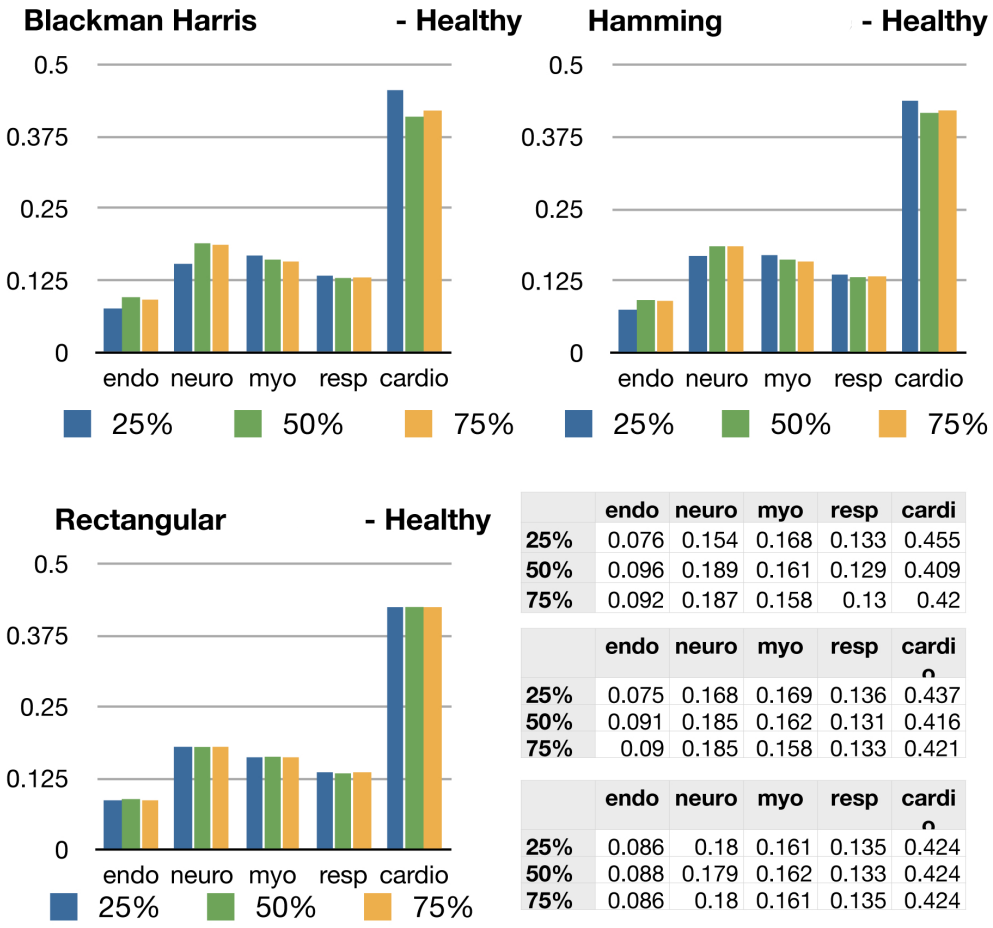

	endo	neuro	myo	resp	cardi
25%	0.076	0.154	0.168	0.133	0.455
50%	0.096	0.189	0.161	0.129	0.409
75%	0.092	0.187	0.158	0.13	0.42

	endo	neuro	myo	resp	cardi
25%	0.075	0.168	0.169	0.136	0.437
50%	0.091	0.185	0.162	0.131	0.416
75%	0.09	0.185	0.158	0.133	0.421

	endo	neuro	myo	resp	cardi
25%	0.086	0.18	0.161	0.135	0.424
50%	0.088	0.179	0.162	0.133	0.424
75%	0.086	0.18	0.161	0.135	0.424

Figure 3.15: Different window functions and overlapping percentages for the high power probe, Healthy Group.

From these two tables we find that differences between different overlaps (within the same window) are small (with $p > 0.05$). However, notice that the p-values at endothelial frequency bands are generally smaller than those from other frequency bands, and especially that the p-values p(25% vs. 50%)<p(25% vs. 75%)<p(50% vs. 75%), e.g, from Table 3.14 we have $0.4084 < 0.5582 < 0.8633$, and in Table 3.15, $0.5582 < 0.7048 < 1$. This confirms that both Blackman Harris and Hamming windows narrows spectrum

in this band, especially with an overlapping of 25%. Next we will calculate the p-values of different window functions with the same level of overlapping.

Table 3.16: p-value for different window functions, same overlapping, **Blackman Harris vs. Hamming**, Group 1, high power probe.

	Endothelial	Neurogenic	Myogenic	Respiratory	Cardiogenic
H25% vs. BH25%	0.8904	0.9451	0.8363	0.8095	0.9725
H50% vs. BH50%	0.8633	0.8094	0.6794	1	1
H75% vs. BH75%	1	1	1	1	1

As with Table 3.14 & 3.15 from Table 3.16 we may conclude with great confidence that the differences induced by different window functions (same overlapping) are small and it is statistically significant (not occurring by chance).

We may choose a variety of different window functions, ranging from low-dynamic-range windows (such as rectangular window) to high-dynamic-range windows (such as Blackman Harris window) and also moderate windows (Hamming), to test the sensitivities of frequency bands within the LDF signals toward different window functions. Although window functions and overlapping percentage indeed have influences on spectral power as we have mentioned before, the p-values we calculated above reveal that these variations are small.

3.4 Summary

In this chapter we briefly described our data sets, e.g., information on measurements, subject information, the statistical test we employed to compare data and the test of normality. Some descriptive statistics were presented before pre-processing and Fourier analysis. These statistics include mean, standard deviation, minimum and maximum values of the LDF blood flux baseline signals, to provide a general overview of the kinds of signal we will analyze.

The pre-processing procedures involve removing undesirable trend and mean, which are necessary to ensure reliable results in the analysis.

We chose estimation of PSD by Fourier transform instead of classical autocorrelation calculation due to Fourier analysis's flexibility and power. PSD by the Welch method is the standard procedure we follow as it's proven to be superior to estimation by periodogram.

We also tested the sensitivities of relative spectral power with different window functions and overlapping percentages. Although there are variations in some frequency bands, the changes are small. p-values reveal these changes are likely to have occurred by chance.

This poses us a question of what kind of window we should use to produce true (or as close as possible) power spectra of LDF signal, and whether there exists a benchmark to make comparisons. There may never be a perfect way to construct the true power spectra of a given signal, however, we can always look for other methods, for example, from Wavelet Analysis we may look at this problem from a different perspective.

In theory, since the high power probe has a greater penetration depth and so possibly samples larger resistance vessels (diameter $> 100\mu m$), these blood vessels are more influenced by heart beat through pulse wave propagation and we should see an increase in cardiogenic activity in the high power probe compared with that in the standard probe. For the healthy group, our analysis shows the cardiogenic activity contributes greatest among all five characteristic frequency bands in the high power probe which samples a greater volume of tissue [12]. However group 1 data do not have this feature. And we also do not see a decrease of cardiogenic activity in the standard probe signal from healthy data, but we do see a decrease of cardiogenic activity from group 1 data. This may suggest that cardiogenic activity in our cohort of individuals with features metabolic syndrome is impaired.

Since our healthy group only contains three data samples, we may need more samples to make meaningful conclusions, by central limit theorem we should increase this number to 30 or more. At this stage, we can only postulate that because the BMI index of group 1 subjects is very high (around 30kg/m^2), i.e., more adipose tissue in the subcutaneous tissue and arterioles and venules are embedded in this layer of tissue, which may undermine LDF measurements in the high power probe. Indeed, for people with obesity, structural changes can lead to altered muscle blood flow [27]. Capillary rarefaction (a reduction in capillary density) is observed in people with obesity and hypertension [21].

On the other hand, for the hyperinsulinemic euglycemic clamp tests, we do not observe statistically significant changes in blood flux from pre to low or high insulin dosages in all five characteristic frequency bands. There is small change in endothelial and cardiogenic activity frequency bands, although $p-$values associated with these do not reach statistical significance at 0.05 level. Our data suggest that in the obesity/insulin resistance cohort studied, hyperinsulinemia does not increase local tissue blood flow.

Chapter 4

Wavelet Analysis

4.1 Introduction

Similar to Fourier analysis described in previous chapters, in this chapter we will analyze LDF blood signals using Wavelet transform. We will perform the following analyses:

- Build 2D and 3D scalogram from continuous wavelet transform (CWT) coefficients of LDF blood signal using complex Morlet wavelet, this is a time-scale (frequency) representation.
- Calculate average scalogram and make comparisons with PSD obtained in Fourier analysis.
- To characterize the dynamics, we calculate relative wavelet spectra (similar to relative spectral power in Fourier analysis) of each characteristic frequency bands.

We use the same data sets, i.e., group 1 ($n = 17$) and healthy group ($n = 3$) for Wavelet analysis. The pre-processing procedures involving detrending, mean removal are also the same as used previously in Chapter 3.

4.2 Scalograms

One of the major advantages of using Wavelet analysis is to obtain a time-frequency representation of a given LDF blood signal. CWT with parameters $f_b = 2$ and $f_c = 1$ is performed on these signals. The convention for choosing $f_c = 1$ is due to the fact that when Jean Morlet formulated this wavelet, he used a constant known as κ_σ, the admissibility criterion. When κ_σ is small,

typically $\kappa_\sigma < 10^-5$, i.e., $\sigma > 5$, we can ignore (simplify) some terms in the original Morlet wavelet. And since $\sigma = 2\pi f_c$, setting $f_c = 1$ is an appropriate trade-off between time-frequency resolutions. The choice of $f_b = 2$ is also a convention used by Jean Morlet and others in the literature [25]. We obtain a matrix of CWT coefficients, and take the absolute values of these coefficients. These absolute values of coefficients are meshed and plotted in two or three coordinates, i.e., time, scale (frequency) and amplitude.

4.2.1 2D Scalogram

An example of 2D a scalogram is illustrated in Fig. 4.1. The 2D scalogram is not as intuitively helpful as the 3D scalogram. The horizontal axis of 2D scalogram is for time and the vertical axis is for scales. It's comparable to the spectrogram based on STFT which is also a time-frequency representation.

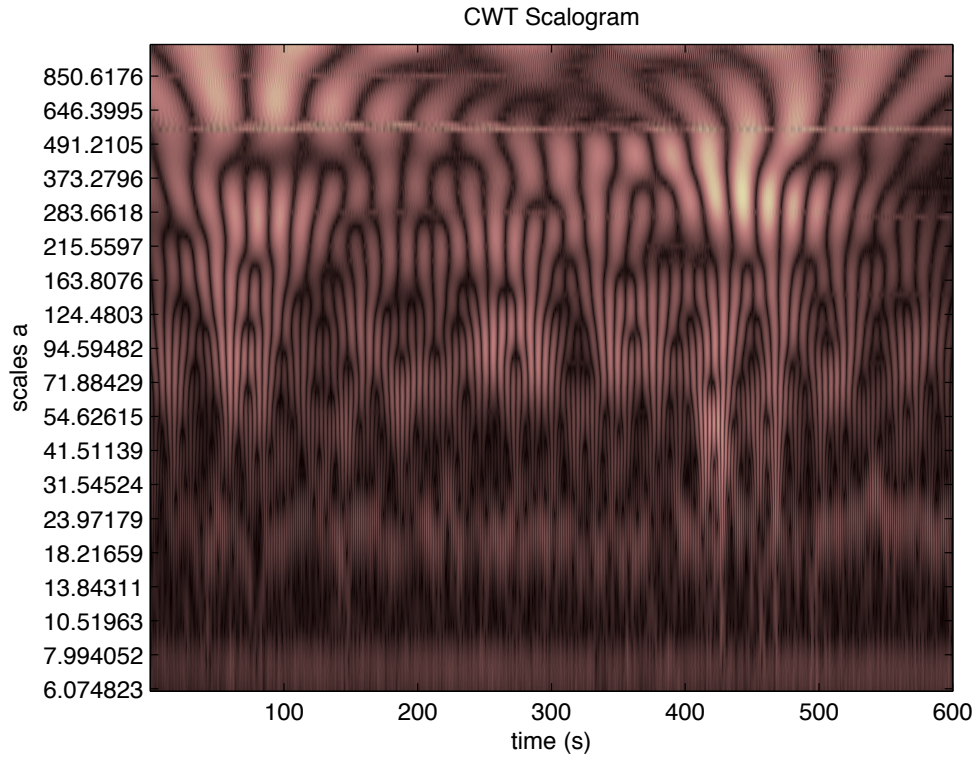

Figure 4.1: 2D Scalogram, a time-scale representation constructed from absolute CWT coefficients.

On the y-axis of this figure are labeled scales, x-axis the time in seconds. In grey-scale plot, brighter portions indicate large values of CWT coefficients. For example, the scales from 6 to 23 are associated with frequencies in the range of 0.4-1.6 Hz or the cardiogenic activity frequency band, we observe a whitened strip at around scales 6 to 7. This can be better visualized in the 3-dimensional scalogram to be introduced below.

4.2.2 3D Scalogram

The 3D scalogram is constructed by adding another quantity, amplitude, to the z-axis. From the 3D scalogram Fig. 4.2 we are able to see at around 1Hz there is a wave-like structure across the time axis, known as the cardiogenic activity, and at around 0.3Hz the respiratory activity, 0.1Hz the myogenic activity and more strikingly at around 0.0095-0.02Hz the endothelial activity. The 3D scalogram is visually more information-rich than the 2D scalogram.

The frequency ranges of the five characteristic bands are labeled in the frequency axis (0.0095-0.02 Hz, 0.02-0.06 Hz, 0.06-0.15 Hz, 0.15-0.4 Hz and 0.4-1.6 Hz). The small peak at around 1 Hz is the cardiogenic activity peak that represents heart beat frequency.

4.2.3 Average Scalogram and PSD

However, we do not just use Wavelet analysis to achieve some visually stimulating figures. We will work out an alternative to the PSD, known as the average scalogram. To construct the average scalogram, we average the absolute wavelet transform amplitude at each scale, and present it in a two-axis figure, one axis being the scale (frequency), the other axis being the (averaged) amplitude. And this is compared with PSD obtained from FFT. This is illustrated in Fig. 4.3. Data used for computing the average scalogram and PSD is from one of the subjects in group 1.

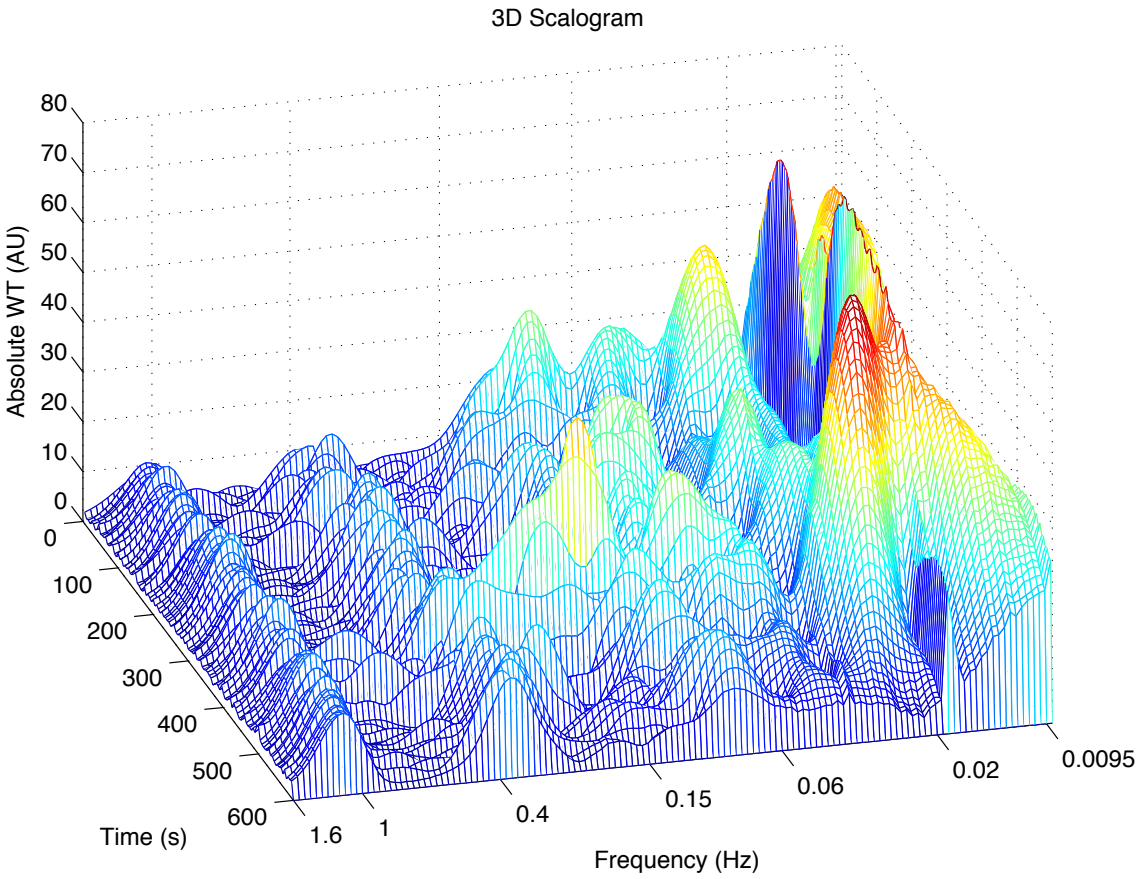

Figure 4.2: 3D Scalogram constructed from absolute CWT coefficients.

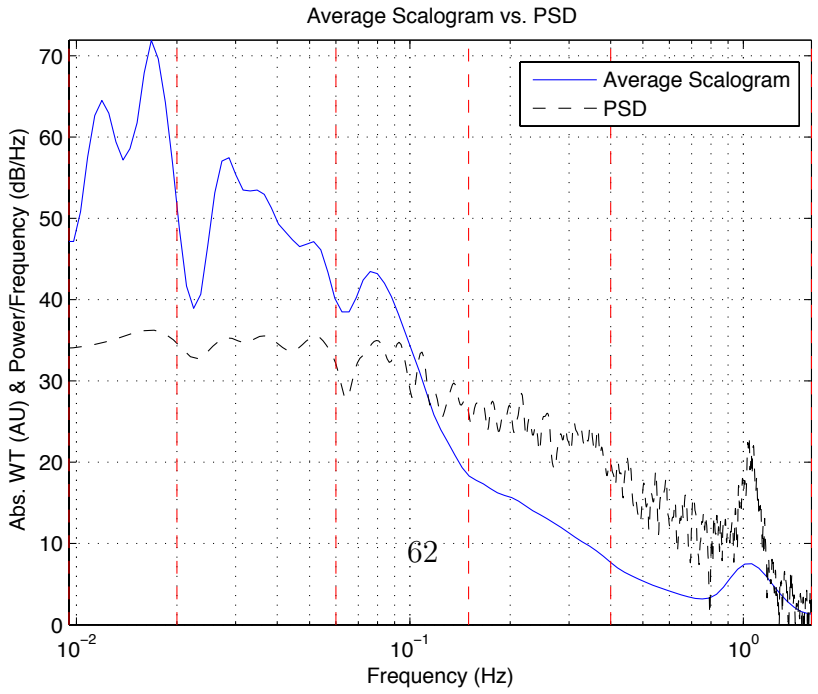

Figure 4.3: Average Scalogram constructed from absolute CWT coefficients vs. PSD from FFT of a signal measured by the high power probe.

In this figure, the five characteristic frequency bands are separated by red dotted lines.

The average scalogram is similar to the PSD. However, because they are estimated from two different mathematical transforms, they do not have comparable units for us to make direct comparisons. Therefore the y-axis of Fig. 4.3 is labeled both in AU (arbitrary unit) and power per frequency dB/Hz (a PSD unit).

Through visual inspection, we are able to tell some differences between the two. We only get a general trend in the PSD for frequencies smaller than 0.4 Hz, the details are very minimal. While for the average scalogram, peaks in each characteristic frequency bands are distinctly demonstrated, i.e., we can spot the myogenic activity (0.06-0.15 Hz) peak at around 0.08 Hz; the neurogenic activity (0.02-0.06 Hz) peak at around 0.03 Hz; and finally the peaks within the endothelial activity bands.

On the other hand, the cardiogenic activity peak is small compared with the other band peaks and not as distinct as that in the PSD. This shows that wavelet analysis has the advantage of having very good frequency resolutions for lower frequency content (endothelial, neurogenic and myogenic activities) and comparably poor frequency resolution for higher frequency content (cardiogenic activity).

4.3 Analysis

4.3.1 Overview

Now that we can construct the average scalogram for each individual LDF signal, we proceed to calculate the relative wavelet spectral power of each characteristic frequency band. The procedure is similar to what we have employed for the PSD, i.e., using trapezoidal numerical integration.

We first compute insulin-specific relative wavelet spectral power for Group 1 data sets to investigate the effects of insulin on skin blood perfusions. We then compute for each group the relative wavelet spectral power for both the wide and standard probes. p-values will be calculated to establish differences between the two methods.

The results are summarized in Table 4.1 for group 1, Table 4.2 for group

2 and Table 4.3 for the healthy group. Box-plots are presented in Fig. 4.4, 4.5 and 4.6 respectively. The major and most striking difference between box-plots produced by Wavelet analysis box-plots produced by Fourier analysis is that lower frequency components (0.0095 - 0.15 Hz) have better frequency resolution, and high frequency components (0.15 - 1.6 Hz) are relative suppressed. As can be shown in the following figures, the cardiogenic and respiratory activities are not very notable in Wavelet analysis.

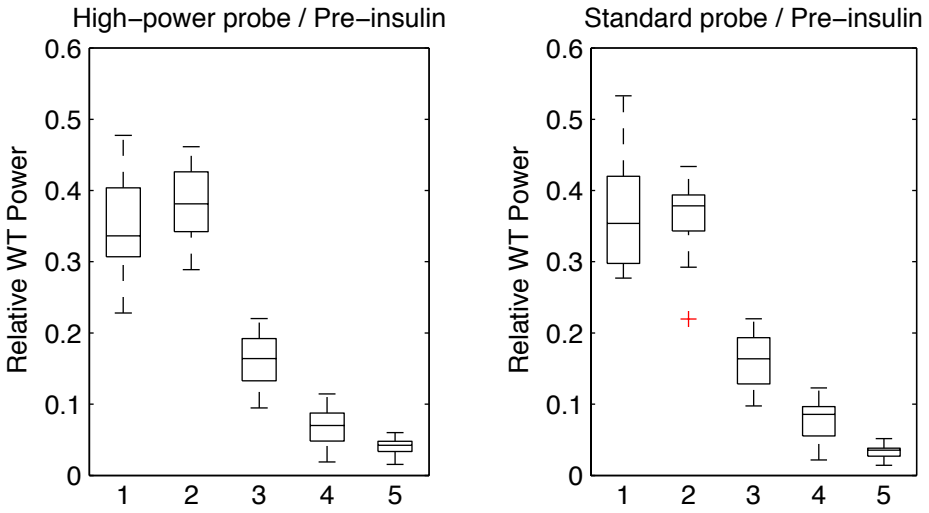

Figure 4.4: Relative wavelet spectral power, Group 1, high-power / standard probes, pre-insulin.

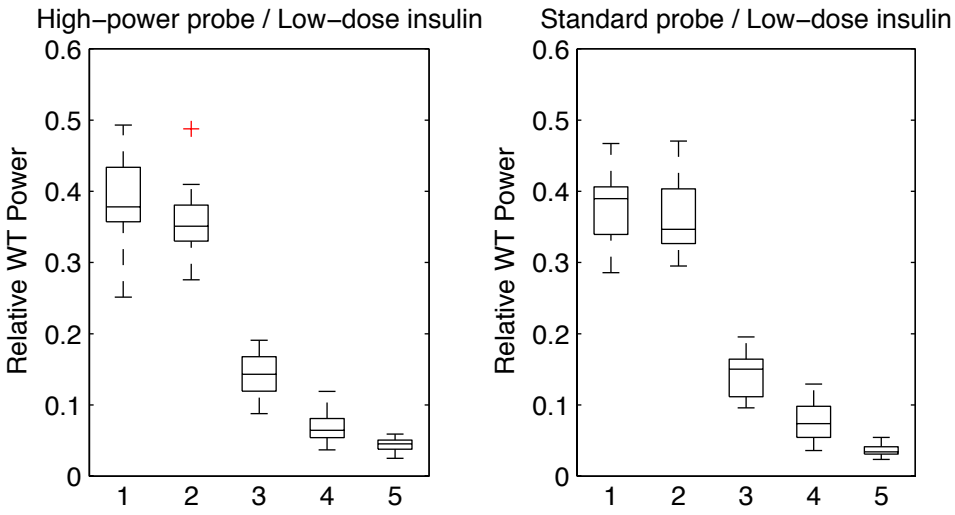

Figure 4.5: Relative wavelet spectral power, Group 1, high-power / standard probes, low-insulin.

The differences between pre-insulin and low-dose insulin signals are observable in that the endothelial activity is increased after low-dose insulin infusion, and comparatively the neurogenic activity is slightly suppressed. Prior to insulin infusion (pre-insulin), the neurogenic activity is slightly more dominant than other activities. Cardiogenic activity is slightly stronger when measured from high-power probes.

As also can be seen in the following figures, respiratory activity measured from high-power probe in the healthy cohort is more notable than that measured from standard probe. On the other hand, neurogenic activity is stronger when measured from standard probe.

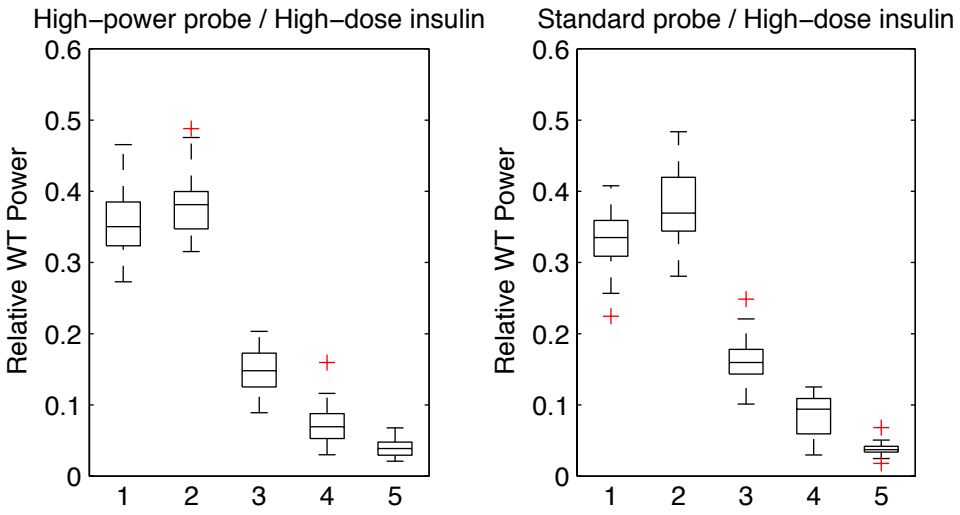

Figure 4.6: Relative wavelet spectral power, Group 1, high-power / standard probes, high-insulin.

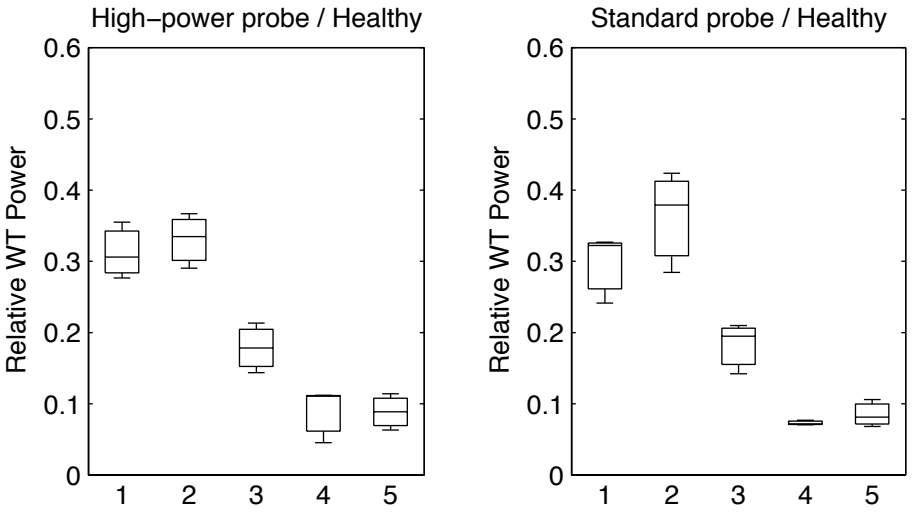

Figure 4.7: Relative wavelet spectral power, Healthy Group, high-power / standard probes, without insulin.

Fig. 4.4, 4.5, 4.6 and 4.7 are box-plots summarizing the statistics of

relative wavelet powers of the five frequency bands. These results are not directly comparable to PSD obtained because although Wavelet Transform has very good frequency resolution for lower frequency components, it has poor frequency resolution for higher frequency components within a signal. This makes WT ideal for analyzing low oscillations in a physiological signal, but potentially biases average scalogram estimates at higher frequencies. However, we are still able to utilize average scalogram for analysis within the Wavelet analysis framework.

Table 4.1: p-values for comparing pre, low, high insulin dosages, Group 1 wide probe.

	endo	neuro	myo	resp	cardio
pre vs. low	0.2557	0.2280	0.1212	0.9177	0.3524
pre vs. high	0.9451	0.7566	0.3524	0.7566	1
low vs. high	0.1055	0.1212	0.4909	0.8363	0.2150

Table 4.2: p-values for comparing pre, low, high insulin dosages, Group1 standard probe.

	endo	neuro	myo	resp	cardio
pre vs. low	0.5353	0.7566	0.2025	0.8633	0.6297
pre vs. high	0.1792	0.5353	0.8904	0.4084	0.2025
low vs. high	0.0192	0.3015	0.1480	0.3892	0.3348

Table 4.3: p-values for comparing G1 pre-insulin and Healthy measurements, wide probe.

	endo	neuro	myo	resp	cardio
pre vs. low	0.2898	0.1384	0.3971	0.3408	0.0081

Table 4.4: p-values for comparing G1 pre-insulin and Healthy measurements, standard probe.

	endo	neuro	myo	resp	cardio
pre vs. low	0.1688	0.9157	0.2898	0.4587	0.0081

As with analysis made in the Fourier Analysis section, for hyperinsulinemia tests, all calculated p-values are greater than 0.05. Therefore statistical analysis performed within the Wavelet analysis framework confirmed the result obtained in the Fourier analysis framework, i.e., no observed change in blood flow under the effect of insulin dosages (low and high).

For comparing healthy group with group 1, p-values in the cardiogenic activity frequency band is the same as the result we obtained in FFT analysis (both $p = 0.0081$). However, p-value for endothelial activity frequency band is greater than 0.2898, this is different from the FFT analysis ($p < 0.05$).

4.4 Summary

In this chapter we used Wavelet transform as a framework for analysis and performed similar tests, constructed models based on scalogram (2D, 3D and Average Scalogram). The 2D and 3D scalograms are time-frequency representations. They enable us to simultaneously view the signal in both time and frequency domains. The average scalogram is similar to PSD, it characterizes the average wavelet power contained in a signal. From the average scalogram we calculated the statistics of relative wavelet power contributions for each of the 5 characteristic frequency bands.

We have shown that the average scalogram is superior at displaying information at lower frequency range, i.e., 0.0095-0.15 Hz covering the endothelial, neurogenic and myogenic activities, compared with a standard PSD model. However, the cardiogenic activity amplitude estimated in the average scalogram tends to be small, this may be due to the intrinsic properties of Wavelet transform, i.e., very good frequency resolution for lower frequencies, poor frequency resolution for higher frequencies (in other words, very good time resolution for the higher frequencies). We will exploit this feature of Wavelet transform in the next chapter to analyze the signal in a energy time-evolution

perspective.

p-values are calculated for results obtained in this Wavelet framework, and are in general agreement with $p-$values obtained in the Fourier framework. These p-values are summarized in tables in the above section.

In short, Wavelet analysis is an alternative to the traditional Fourier analysis. It is only superior in resolving lower frequency components contained in a signal. It is also a time-frequency representation, which can enable us to look at the signal in both time and frequency domains. It is an invaluable tool for biomedical signal processing.

Chapter 5

Time-energy Evolution

5.1 Introduction

With models based on FFT, we lose information on the time domain entirely, for example the PSD contains only frequencies and amplitudes. A joint time-frequency representation such as STFT, WT, EMD (empirical mode decomposition) or WVD (Wigner-Ville distribution) may help solve this problem by adding another dimension to aide the analysis. We argued that Wavelet analysis has superiority in resolving lower frequency components over STFT, and we are interested in knowing how the endothelial activity frequency band energies evolve in time and we construct a new model to examine this.

The 3D scalogram contains characteristic frequency peaks in the frequency axis, these peaks also have varying amplitudes in the time axis. There are more peaks in the time axis for higher frequency components, e.g., the cardiogenic activity, and far fewer peaks for the endothelial activity. This is the first impression we get when visualizing the 3D scalogram.

We will briefly describe a time-evolution model based on this notion. Based on this time-evolution model, we will analyze particularly the endothelial activities during pre, low and high-insulin measurements.

5.2 Temporal Frequency

5.2.1 Model Overview

The time-energy evolution model proposed here is a continuation from Wavelet analysis we performed in a previous chapter. The motivation is that instead of looking at the wavelet frequency spectrum as a whole in terms of time, we look at the average absolute wavelet transform of each frequency band against time. For example, for the endothelial activity band, we average the absolute CWT in the frequency range 0.0095-0.02 Hz and plot it against time. This is can be illustrated in Fig. 5.1.

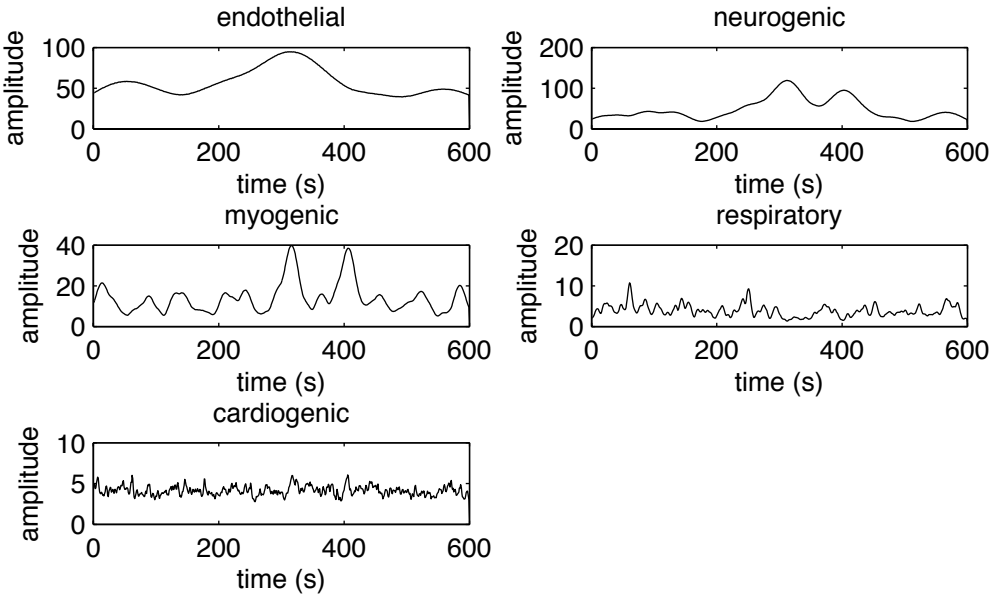

Figure 5.1: Time-Energy evolution of five characteristic bands.

For a signal length of 600s, we expect a lot of oscillatory fluctuations happening in the cardiogenic activity frequency band, as is confirmed in Fig. 5.1, the same can be said for respiratory activity.

The sinusoid-like shape of these oscillations suggests that each activity frequency band may contain multiple oscillations that are under the influence of multiple mechanisms. Whether they are unknown or these oscillations influence each other, we do not know the dynamics. However, based on this

model, we compare the effects of insulin dosages on blood flux at this particular band - endothelial activity. This may help us to gain insights on how hyperinsulinemia specifically affects the endothelial activity.

Spike-induced Ripple Effect

From constructing this time-evolution model, we find that spikes have a large rippling effect on the endothelial activity. Often LDF blood flux signals are subject to body movement or other artifacts of unknown sources, this may be presented in Fig. 5.2 with two spikes at around 140s and 160s.

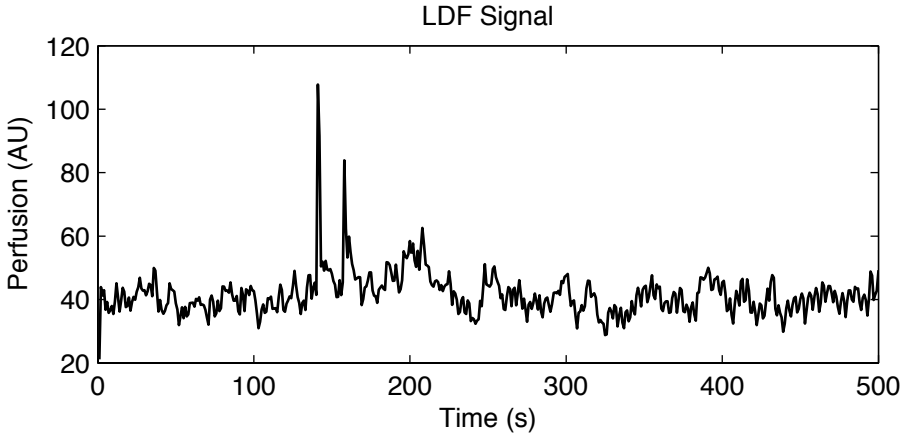

Figure 5.2: A LDF Signal with some spikes.

For this signal, we plot the time-evolution for each of the five frequency bands, see Fig. 5.3.

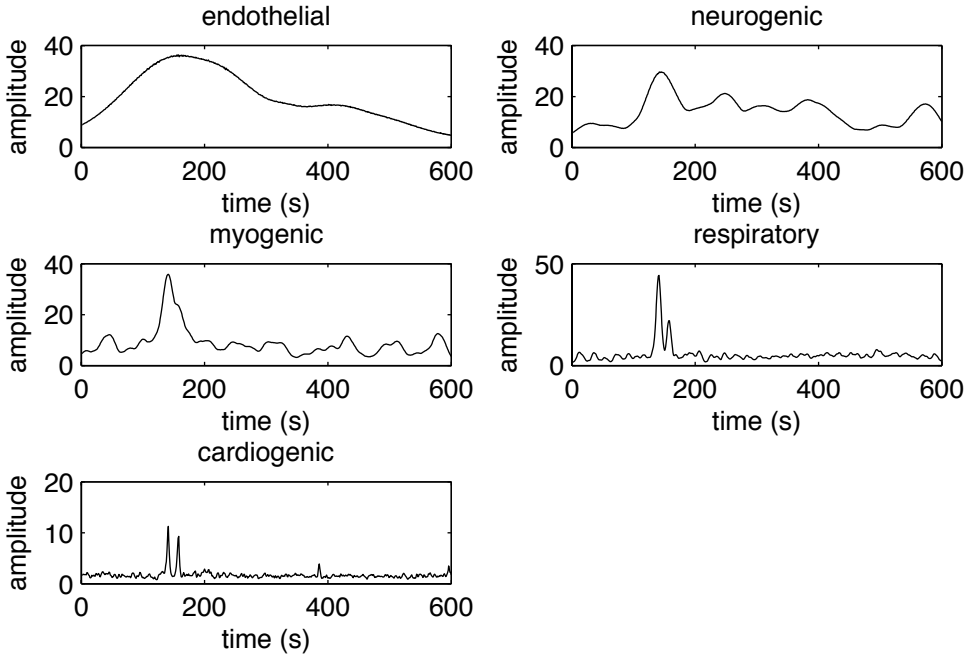

Figure 5.3: Time-Energy evolution of all frequency band, without insulin, high power , G1

These two spikes correlate with activities of all five frequency at around 140s and 160s as shown in Fig. 5.3, the ripple effect of this spike on endothelial band is most notable. These effects are likely the consequence of artifacts on our analysis methods, i.e., wavelet transform. Also observe that in different frequency bands, as reflected in Fig. 5.3, the consequence of this effect is amplified, likely a result of dilating and shifting wavelet functions.

5.2.2 Endothelial Activity

We will show that a typical endothelial activity band-specific time evolution (for pre, low and high insulin measurements) in Fig. 5.4 where the black, blue and red lines are for the pre, low and high insulin measurements respectively.

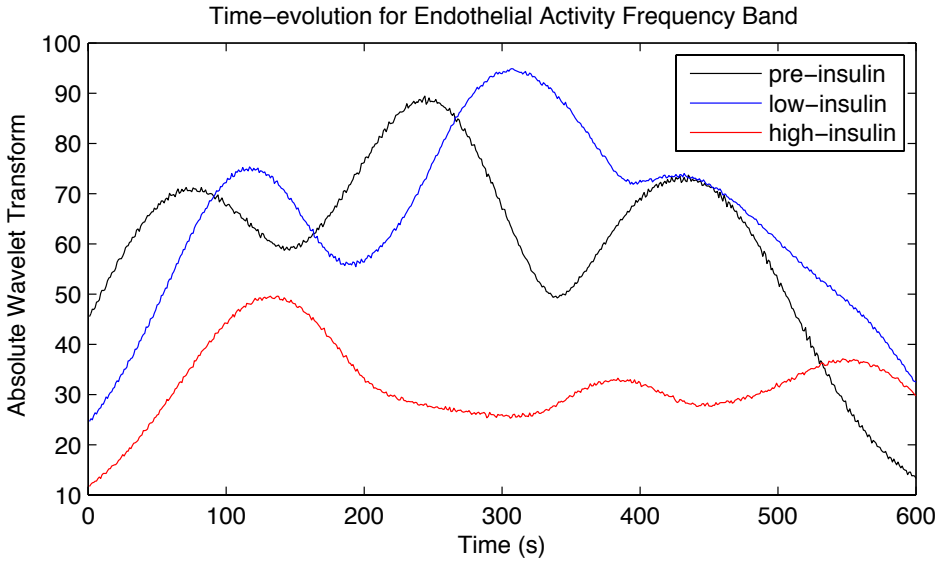

Figure 5.4: Time-Energy evolution of endothelial activity frequency band for typical pre, low and high insulin measurements.

In Fig. 5.4, we are seeing that these measurements vary in both amplitudes and frequency of oscillations. For example, the following observation in terms of their local maxima can be made. The pre-insulin curve reaches a local maximum at around 70s while the low-insulin reaches a local maximum at around 105s. There seems to be a shift of another 70s when both pre-insulin and low-insulin curves reach their respective second local maximum at around 230s and 300s. They both reach a third maximum at around 430s.

There are many aspects one may wish to analyze. Average absolute wavelet transform (amplitude) can be calculated to determine which of pre, low, high-insulin measurements has the highest amplitude in this band. Integration of the absolute wavelet spectrum can be used to obtain the amount of energy contained in each measurement. Local maxima may be associated with physiological changes of state, e.g., a change in endothelial response mediated by insulin.

5.2.3 Analysis

Under normal physiological conditions for healthy people, we would see an increase in skin blood flux power in the endothelial frequency band from

pre to low-insulin dosage, and from low to high-insulin dosage. Based on this notion and the time-evolution model, we calculate the mean amplitudes endothelial activity of pre, low and high dose insulin measurements of all subjects in group 1 ($n = 17$).

No.	Pre-insulin	Low-insulin	High-insulin	Pre->Low	Low->High
1	57.08	65.67	57.89	115.04%	88.16%
2	83.59	65.08	97.44	77.87%	149.72%
3	73.19	34.97	60.87	47.79%	174.05%
4	50.47	86.88	88.21	172.12%	101.53%
5	42.76	50.55	49.92	118.21%	98.76%
6	49.77	30.18	48.12	60.63%	159.46%
7	39.10	39.23	28.63	100.33%	72.98%
8	30.20	38.67	50.65	128.05%	130.99%
9	136.22	60.07	136.72	44.10%	227.60%
10	25.29	24.02	32.75	95.00%	136.32%
11	27.79	36.78	19.20	132.36%	52.19%
12	60.90	65.46	32.16	107.48%	49.13%
13	66.15	55.44	47.23	83.81%	85.20%
14	66.35	79.47	71.25	119.77%	89.65%
15	28.41	29.07	35.93	102.32%	123.60%
16	60.35	48.96	45.66	81.13%	93.25%
17	45.73	45.66	61.48	99.84%	134.63%

Figure 5.5: Average WT amplitude at endothelial activity frequency band of all 17 subjects, Group 1, and proposed endothelial insulin function classification.

As we have already concluded in Chapter 3 and 4, that in this cohort of obese and insulin-resistant individuals, there is no change of blood flux in response to hyperinsulinemia. Fig. 5.5 summarizes the calculated mean amplitudes. Given the sample size for the analysis we may not be able to draw any definitive conclusions. We can only conclude by reporting that based on our model, only two subjects show corresponding increase in mean amplitudes (in endothelial activity) in response to both low and high dose insulin. The remaining 15 subjects show abnormal endothelial activity.

5.3 Sinusoidal Fitting

5.3.1 Introduction

We realize that the insulin curves in the time-evolution model resemble superpositions of sinusoidal functions. Sinusoidal functions have long been used to study vibrations and oscillations. For example, $\sin(px)$ has frequency $p/2\pi$ and period $2\pi/p$. We are able to fit the endothelial activity curves of the time-evolution model into a sum of multiple sinusoidal functions and this scheme may help us understand the nature of these oscillations. For example, in Fig. 5.6 we fit a pre-insulin curve (purple) with multiple sinusoidal functions (red) with 8 sinusoids to considerable degree of accuracy, in the form of $f(x) = a_1 \sin(b_1 x + c_1) + a_2 \sin(b_2 x + c_2) + \cdots + a_8 \sin(b_8 x + c_8)$. We then summarize our findings by collecting statistics about the fitted parameters, mainly a_1 the dominant amplitude and its associated frequency b_2.

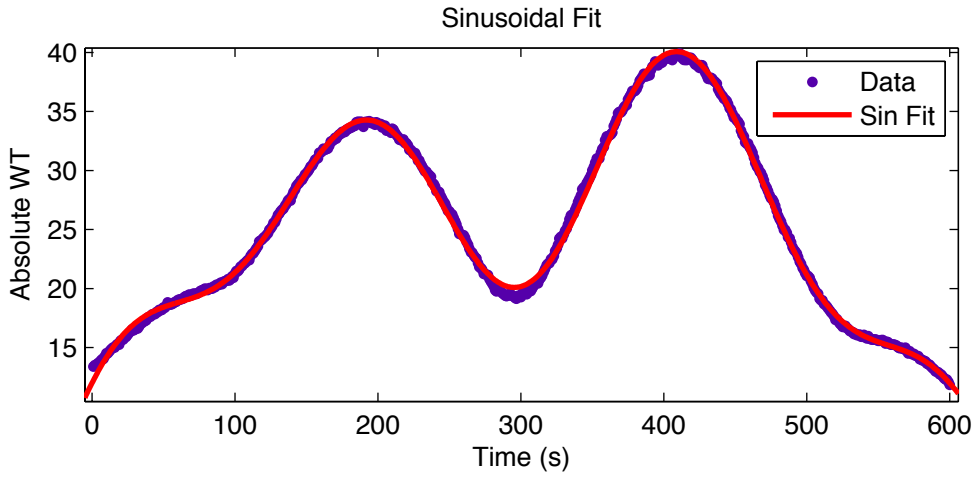

Figure 5.6: Fitting using multiple sinusoidal wave.

For example, a fit of curve with 3 sinusoids may be expressed analytically as

$$f(x) = 32.07 \sin(0.00408x + 0.2972) + \tag{5.1}$$
$$6.509 \sin(0.01863x - 0.5116) + \tag{5.2}$$
$$5.794 \sin(0.03131x + 1.514) \tag{5.3}$$

with three oscillations: 0.00065 Hz, 0.003 Hz and 0.005 Hz. On the other hand, for a low-insulin curve (from the same subject), we have the following result:

$$f(x) = 32.57\sin(0.004216x + 0.5574)+ \tag{5.4}$$
$$8.154\sin(0.01578x - 1.267)+ \tag{5.5}$$
$$3.412\sin(0.02711x - 4.129) \tag{5.6}$$

with three oscillations: 0.0067 Hz, 0.0025 Hz and 0.0043 Hz. The corresponding high-insulin curve has the following fit:

$$f(x) = 42.94\sin(0.004023x + 0.7096)+ \tag{5.7}$$
$$16.05\sin(0.01775x - 1.382)+ \tag{5.8}$$
$$6.438\sin(0.02933x - 3.3129) \tag{5.9}$$

with three oscillations: 0.00064Hz, 0.0028Hz and 0.0047Hz.

Table 5.1: Goodness of Fit

SSE	R-Square	Adjusted R-Square	RMSE
69.72	0.9981	0.9981	0.3435
723.5	0.988	0.9878	1.106
380.4	0.997	0.997	0.8023

where SSE is the sum of squared errors and RMSE is the root mean square error, two commonly used measures for the difference between observed data and values predicted by model.

The fitted function contains three parameters: amplitude, phase, and frequency. Therefore we should note these oscillations are under the influence of these three parameters. Each fitted function contains a dominant amplitude a_1, a less dominant a_2, and a least dominant a_3. We will introduce a fitting scheme in the next section.

5.3.2 Fitting Scheme and Results

We fit each insulin curve with 8 sin functions to obtain as close a fit as possible. Often a 3-sin fit is sufficient to ensure a good fit. We will compare

the oscillatory changes of the two most dominant terms which contain the largest two amplitudes , i.e., a_1 and a_2 for pre, low, and high insulin curves of 17 data sets from group 1 (cohort of individuals with features of metabolic syndrome).

Results (group 1 data)

The fitting results (high power probe data) are summarized in Table 5.2

Table 5.2: Fitted parameters of the first 8 data sets for group 1 using 8-sin fit. High power probe.

No.	a_1	b_1	c_1	a_2	b_2	c_2
1. pre	94.5273	0.0053	0.4153	25.2028	0.0095	1.8760
1. low	115.7317	0.0053	0.1177	57.0701	0.0093	2.5914
1. high	77.6010	0.0048	0.1196	31.4393	0.0123	0.9151
2. pre	131.6	0.0035	0.4976	44.4184	0.0129	0.7257
2. low	82.2030	0.0040	0.4002	23.7412	0.0200	1.4650
2. high	131.6689	0.0044	0.3753	13.9136	0.0179	0.0006
3. pre	107.0551	0.00386	0.4811	40.1183	0.0705	7.3300
3. low	54.3792	0.0035	0.4217	25.6257	0.0070	2.9644
3. high	75.6526	0.0040	0.4178	63.7699	0.0123	0.7064
4. pre	64.0079	0.00388	0.3222	39.7140	0.0208	4.7835
4. low	131.0495	0.0044	75.9775		0.0086	3.1866
4. high	127.4031	0.0042	0.0002	34.7773	0.0062	1.5488
5. pre	57.8146	0.0038	0.8641	18.1619	0.0174	4.4896
5. low	79.7443	0.0056	0.1392	51.5632	0.0133	1.1190
5. high	65.8649	0.0045	0.0311	34.8355	0.0115	1.4586
6. pre	50.3905	0.0053	0.4387	36.8328	0.0132	1.8141
6. low	43.3261	0.0046	0.3976	7.0184	0.0160	2.7745
6. high	76.7233	0.0048	0.4778	8.3260	0.0181	1.8099
7. pre	66.1956	0.0050	0.1286	34.5953	0.0089	2.2902
7. low	57.4093	0.0044	0.4262	19.4187	0.0148	4.5236
7. high	41.9206	0.0053	0.0004	20.6267	0.0117	1.1663
8. pre	50.3905	0.0053	0.0057	10.2174	0.0191	0.5795
8. low	51.2200	0.0050	0.0105	24.9633	0.0113	1.4503
8. high	73.9815	0.0054	0.3016	52.5505	0.0127	0.5540

Table 5.3: Fitted parameters of the last 9 data sets for group 1 using 8-sin fit. High power probe.

No.	a_1	b_1	c_1	a_2	b_2	c_2
9. pre	189.7833	0.0043	0.4477	75.3044	0.0098	2.0060
9. low	84.0428	0.0049	0.0015	35.0979	0.0114	1.0056
9. high	225.1587	0.0052	0.0002	76.8568	0.0097	2.1529
10. pre	36.6088	0.0051	0.0006	8.6990	0.0137	0.6469
10. low	38.5638	0.0056	0.1429	17.1560	0.0146	0.5443
10. high	38.2595	0.0064	0.1564	17.8286	0.0107	0.9318
11. pre	44.9962	0.0043	0.0680	22.4971	0.0083	1.7307
11. low	56.8093	0.0051	0.1397	22.9819	0.0103	2.5082
11. high	28.2497	0.0045	0.3545	6.4727	0.0163	3.1739
12. pre	93.9052	0.0050	0.2319	23.3132	0.0104	1.8827
12. low	99.3106	0.0042	0.3704	19.4576	0.0064	3.2626
12. high	48.5839	0.0043	0.4618	13.9370	0.0111	1.5232
13. pre	89.2567	0.0043	0.4255	58.9435	0.0096	2.9390
13. low	84.3052	0.0047	0.4898	60.5712	0.0084	3.5575
13. high	66.4526	0.0045	0.0032	13.9472	0.0186	1.7621
14. pre	95.7718	0.0047	0.1969	16.1647	0.0125	0.0008
14. low	120.0742	0.0039	0.4675	54.8379	0.0076	2.6576
14. high	113.4608	0.0047	0.2128	44.6584	0.0077	2.9785
15. pre	63.1746	0.0041	0.4500	34.9075	0.0054	3.4642
15. low	46.0202	0.0047	0.4290	22.9877	0.0097	1.9764
15. high	53.9877	0.0046	0.2688	25.9289	0.0089	2.3732
16. pre	85.5007	0.0047	0.2334	38.4016	0.0104	1.1657
16. low	74.9541	0.0049	0.2385	24.5957	0.0100	1.5535
16. high	76.6451	0.0051	0.2182	14.9592	0.0241	0.8367
17. pre	68.7240	0.0049	0.1856	22.2248	0.0101	1.6487
17. low	65.3792	0.0050	0.0411	26.7635	0.0114	1.4129
17. high	69.7175	0.0046	0.2815	25.6429	0.0110	1.1841

It can be observed that values of amplitudes a_1, a_2 fluctuate, while values of the b_1 term do not vary as much. The mean and standard deviation for the above data as well as data from the standard probe are formulated in Table. 5.4, 5.5, 5.6, 5.7.

Table 5.4: Mean (μ) for the fitted parameters (group 1). High power probe.

mean	a_1	b_1	c_1	a_2	b_2	c_2
pre	80.8201	0.0045	0.2924	30.3470	0.0118	1.7996
low	75.5601	0.0047	0.2774	33.5193	0.0109	2.2678
high	81.8430	0.0048	0.2165	29.4394	0.0130	1.4751

Table 5.5: Standard deviation (σ) for the fitted parameters (group 1). High power probe.

std dev.	a_1	b_1	c_1	a_2	b_2	c_2
pre	35.1565	0.0006	0.2311	18.5901	0.0047	1.2087
low	28.0122	0.0006	0.1794	19.0668	0.0034	1.0655
high	46.8746	0.0006	0.1697	19.9967	0.0046	0.8450

Statistics for data sets measured from standard probe (skin) are summarized in the following tables:

Table 5.6: Mean (μ) for the fitted parameters (group 1). Standard probe.

mean.	a_1	b_1	c_1	a_2	b_2	c_2
pre	12.0739	0.0046	0.3151	5.5887	0.0125	1.9434
low	10.0568	0.0046	0.3276	5.2279	0.0128	2.3145
high	7.8923	0.0045	0.2869	3.1730	0.0129	1.5558

Table 5.7: Standard deviation (σ) for the fitted parameters (group 1). Standard probe.

std dev.	a_1	b_1	c_1	a_2	b_2	c_2
pre	9.2604	0.0009	0.3515	5.5608	0.0051	1.1841
low	5.3061	0.0009	0.3170	4.7570	0.0060	1.2071
high	3.0411	0.0006	0.2326	1.5766	0.0047	1.2558

Results (group 2 data)

The 12 sets of fitted parameters for group 2 data are obtained in a similar way as for group 1 data and are hence omitted here for displaying. The mean and standard deviation are summarized in the following tables.

Table 5.8: Mean (μ) for the fitted parameters (group 2). High power probe.

std dev.	a_1	b_1	c_1	a_2	b_2	c_2
pre	83.5124	0.0049	0.1805	34.6813	0.0114	1.6539
low	101.9574	0.0046	0.1663	36.7413	0.0134	1.1796
high	74.8012	0.0047	0.2635	27.8534	0.0105	1.9184

Table 5.9: Standard deviation (σ) for the fitted parameters (group 2). High power probe.

std dev.	a_1	b_1	c_1	a_2	b_2	c_2
pre	27.8079	0.0005	0.1679	14.7690	0.0038	0.7805
low	93.9438	0.0015	0.1680	23.9048	0.0047	1.1116
high	37.2021	0.0005	0.2209	14.6083	0.0019	0.9133

Table 5.10: Mean (μ) for the fitted parameters (group 2). Standard probe.

std dev.	a_1	b_1	c_1	a_2	b_2	c_2
pre	6.6661	0.0043	0.4153	4.0313	0.0111	2.2557
low	7.6021	0.0042	0.3195	3.1778	0.0178	1.2957
high	6.5560	0.0042	0.3492	3.3166	0.0107	2.0767

Table 5.11: Standard deviation (σ) for the fitted parameters (group 2). Standard probe.

std dev.	a_1	b_1	c_1	a_2	b_2	c_2
pre	4.4071	0.0007	0.3656	4.5696	0.0032	1.3803
low	5.1712	0.0014	0.2317	3.8489	0.0147	1.3326
high	3.5555	0.0014	0.4166	1.8784	0.0030	1.1958

Analysis

For the purpose of simple interpretations of the above results, consider the ratio of standard deviation to mean (σ/μ), summarized in the following table.

Table 5.12: σ/μ ratio for group 1, high power probe data sets.

std dev.	a_1	b_1	c_1	a_2	b_2	c_2
pre	43.50%	13.46%	79.04%	61.26%	39.38%	67.15%
low	37.07%	12.42%	64.48%	56.88%	30.97%	46.98%
high	57.27%	11.98%	78.40%	67.92%	35.20%	57.28%

Table 5.13: σ/μ ratio for group 1, standard probe data sets.

std dev.	a_1	b_1	c_1	a_2	b_2	c_2
pre	76.70%	20.46%	111.6%	99.50%	40.57%	60.93%
low	52.76%	19.62%	96.77%	90.99%	46.49%	52.16%
high	38.53%	13.93%	81.07%	49.69%	36.26%	80.71%

Table 5.14: σ/μ ratio for group 2, high power probe data sets.

std dev.	a_1	b_1	c_1	a_2	b_2	c_2
pre	33.30%	10.74%	93.03%	42.58%	33.52%	47.19%
low	92.14%	32.96%	101.1%	65.06%	35.34%	94.23%
high	49.73%	10.44%	0.5245%	18.31%	47.61%	95.80%

Table 5.15: σ/μ ratio for group 2, standard probe data sets.

std dev.	a_1	b_1	c_1	a_2	b_2	c_2
pre	66.11%	17.09%	88.02%	113.4%	28.34%	61.19%
low	68.02%	33.88%	72.51%	121.1%	82.80%	102.9%
high	54.23%	32.09%	119.3%	56.63%	28.16%	57.58%

The ratio of standard devation to mean is known as the coefficient of variation (CV), is dimensionless, and thus making it easier for us to compare fitted parameters. A lower value of CV implies a good fit of model. Observe that b_1s are very similar in value (the mean does not fluctuate much) and this is reflected by the lower values of CV. This gives us a hint that the dominant amplitude is modulated by a frequency that's in the range of 0.0042 rad/s to 0.0049 rad/s for all fitted data sets. However, we do not know whether this modulation is of a physiological nature or of some other sources. This is an interesting observation from the model we've set up so far that's based on the Wavelet analysis framework we described in a previous chapter.

For b_1s in Table 5.4, the student-t test reject the null hypothesis at 0.05% significance level for a mean μ of 0.0382 to 0.00474 (confidence interval), such a value is in the 95% confidence interval on the mean of the sample. The next table summarizes 95% confidence intervals.

Table 5.16: 95% confidence intervals for selected fitted parameters. Group 1, high power/standard probes.

high	b_1	b_2	std	b_1	b_2
pre	0.0038-0.0047	0.0094-0.0142		0.0041-0.0050	0.0099-0.0151
low	0.0033-0.0051	0.0091-0.0126		0.0041-0.0051	0.0097-0.0159
high	0.0034-0.0051	0.0106-0.0154		0.0042-0.0048	0.0105-0.0153

Table 5.17: 95% confidence intervals for selected fitted parameters. Group 2, high power/standard probes.

high	b_1	b_2	std	b_1	b_2
pre	0.0045-0.0052	0.0090-0.0138		0.0038-0.0047	0.0091-0.0131
low	0.0036-0.0056	0.0104-0.0164		0.0033-0.0051	0.0084-0.0271
high	0.0044-0.0051	0.0093-0.0117		0.0034-0.0051	0.0088-0.0126

5.4 Summary

We have shown in this chapter, within the Wavelet analysis framework that we are able to look at the LDF signal from a different perspective, the time energy evolution of all five frequency bands. We focus especially on the endothelial band, thanks to Wavelet transform's ability to obtain very good frequency resolution for lower frequency components.

For signals that contain spikes, large ripple effects can be observed on each of the frequency band, especially on the endothelial band, as shown in Fig. 5.3. The origin of these spikes is unknown. For a signal that seemingly contains no obvious artifact, e.g., Fig. 5.1, we also observe spikes in each frequency band in a time-synchronous manner, e.g., there are two notable spikes in the myogenic activity band at around 350s and 410s, the corresponding pair spikes can also be found in the neurogenic band. We would perhaps need to know the dynamics that influence these five frequency bands before being able to properly interpret this phenomenon. At this present stage, we can only use Wavelet analysis for observations that we otherwise can hardly discern.

The parameter (average WT amplitude) calculated from the this time-evolution model, and the criteria used may be helpful in identifying whether a subject has abnormal insulin function, e.g., insulin resistance. We observe that 15 out of the 17 subjects who have features of metabolic syndrome have abnormal insulin function. We cannot achieve this just from time domain analysis of LDF signals.

In the end, the time-evolution curve for the endothelial activity frequency band is fitted with multiple sin functions. Sin functions have been used to study oscillations and vibrations, the multiple (we used 8) sin function can

be fitted to our data to very good accuracy. There are three parameters associated with the shapes (or time-evolution) of these oscillations: amplitude, phase, and frequency. The dominant sinusoidal term has a fitted frequency of approximately 0.005 rad/s, but we do not know the physiological origin of this frequency, the less dominant term has a oscillatory frequency of approximately 0.01 rad/s to 0.03 rad/s. We understand that these frequencies are different from the physiological frequency band of the endothelial activity, i.e., 0.0095-0.02Hz or the slower oscillation 0.005-0.0095Hz which may be related to the endothelium-derived hyperpolarizing factor mechanism. This is because we are assessing the temporal change of WT amplitude (or energy), not the temporal change of the signal itself.

Chapter 6

Conclusions

Both Fourier analysis and Wavelet analysis based approaches can be used to investigate control of tissue perfusion under physiological and pathophysiological conditions. This is shown in PSD and average scalogram's sensitivity in detecting the five characteristic frequency bands in the frequency domain. These approaches can be used together with statistics to characterize changes in blood flow both at rest and in response to hyperinsulinemia euglycemic clamp test.

6.1 Limitations

6.1.1 LDF

The non-invasiveness and continuous recording of skin blood flow for long duration have made LDF an invaluable tool for assessing microcirculation of human skin [13]. Motion artifacts are still a problem that can easily contaminate LDF signals as well as temporal variations. The arbitrary unit of signals is also one of the major limitations of LDF, and it has been suggested to take the more physiological method of expressing data as conductance (AU/mm Hg), i.e., flux over blood pressure. However, our experiments lacked measurements of real-time arterial pressure.

6.1.2 Sample size

Our sample is perhaps a bit small to obtain significant results, e.g., we only have 3 data sets for the healthy subjects and 2 groups (one with 17, another with 12) of data sets for a cohort of subjects with features of metabolic syndrome. For a small sample size, we may be constrained in having limited

preciseness in estimating model parameters. The problem is that for large sample size, the mean will approximate a normal distribution. For a small sample size, this may not be the case. An in-depth power analysis and experimental design may be required in future studies.

6.2 Remarks on Signal Analysis

We observed only slight changes ($p > 0.05$, not statistically significant) of blood flow from pre to low or high insulin dosages for group 1 data sets (metabolic syndrome) from both standard and wide probes. We can notice some changes in the endothelial, cardiogenic activity bands, but calculated $p-$values cannot reject the null hypothesis that two samples have equal mean in the 0.05 level significance, most likely that we will need to increase our sample size.

When comparing healthy subjects ($n = 3$) with group 1 subjects, calculated $p-$values ($p = 0.0343$ for endothelial activity band, $p = 0.0149$ for neurogenic band and $p = 0.0081$ for cardiogenic activity) suggest statistically significant changes in relative spectral powers.

The same results obtained using average scalogram in Wavelet analysis can be in general supported by using PSD obtained from Fourier analysis, this was summarized in Chapter 4.

6.2.1 Fourier Analysis

For Fourier analysis, challenges remain for the post-processing of LDF signals, e.g., we've observed in Chapter 3 that choice of window function has subtle influences on PSD estimation. However, from calculated p-values ($p > 0.05$) we may conclude that there are no statistically significant differences, i.e., variations in mean are very small and are within the 95% confidence interval.

6.2.2 Wavelet Analysis

The analysis of oscillations of endothelial activity band in the time-evolution model is very challenging. We observe oscillatory changes for pre, low and high insulin dosages, but it's very difficult to make physiological interpretations at this stage. However, we did attempt to analyze the oscillatory

changes by fitting multiple sinusoidal functions to these curves, two oscillations are found, one from the dominant amplitude term, about 0.005 rad/s, and the other from the less dominant amplitude term, about 0.0127 rad/s. The result is limited, and leaves spaces for future work.

We also observe suppressed cardiogenic activity power estimated from average scalogram, compared with that estimated by PSD from Fourier analysis. This is in accordance with several other Wavelet applications on LDF signals [8], but we do not know the mathematical origin of this problem, perhaps it's due to Wavelet's poor frequency resolution for higher frequency components.

6.3 Future Work

In the future if opportunities permit, we perhaps could increase our sample size by obtaining more measurements on both MS patients and healthy subjects, and extend measurement duration to improve the reliability of analysis.

Standardized experimental protocols could perhaps minimize temporal variations and motion artifacts, thus increasing overall LDF signal post-processing reliability. For example, cuff inflator with automatic release can minimize movement artifacts at the end of arterial occlusion.

The discrete wavelet transform may have interesting applications (e.g., multi-resolution analysis) for LDF signals if one investigates further. Other signal processing techniques such as empirical mode decomposition, Wigner-Ville distribution may also be studied and used for comparisons with Fourier and Wavelet analysis.

References

[1] SC Agarwal, J Allen, A Murray, and IF Purcell. Comparative reproducibility of dermal microvascular blood flow changes in response to acetylcholine iontophoresis, hyperthermia and reactive hyperaemia. *Physiological Measurement*, 31:1–11, 2010.

[2] Metin Akay. Wavelet applications in medicine. *IEEE Spectrum*, pages 50–56, 1997.

[3] Guy Amit, Noam Gavriely, and Nathan Intrator. Cluster analysis and classification of heart sounds. *Biomedical Signal Processing and Control*, 4:26–36, 2009.

[4] J Arrillaga and N R Watson. *Power System Harmonics*. John Wiley Sons, 2003.

[5] Miriam R Avery, David Voegeli, Christopher D Byrne, David M Simpson, and Geraldine F Clough. Age and cigarette smoking are independently associated with the cutaneous vascular response to local warming. *Microcirculation*, 16:725–734, 2009.

[6] Jeffery C. Bauer. *Statistical Analysis for Decision Makers in Healthcare*. CRC Press, 2009.

[7] Alan Bernjak and Aneta Stefanovska. Importance of wavelet analysis in laser doppler flowmetry time series. *Proceedings of the 29th Annual International Conference of the IEEE EMBS*, pages 4064–4067, 2007.

[8] Maja Bracic and Aneta Stefanovska. Wavelet-based analysis of human blood-flow dynamics. *Bulletin of Mathematical Biology*, 60:919–935, 1998.

[9] Christopher D. Byrne and Sarah H. Wild. *The Metabolic Syndrome and Primary Care*. Wiley, 2007.

[10] C. Carmine, S.S. Nambi, C.M. Kilcoyne, W.K. Choucair, A. Katz, M.J. Quon, and J.A. Panza. Insulin stimulates both endothelin and nitric oxide activity in the human forearm. *Nature*, 332:411–415, 1999.

[11] MG Clark, MG Wallis, EJ Barrett, MA Vincent, SM Richards, LH Clerk, and AS Rattigan. Blood flow and muscle metabolism: a focus on insulin action. *Am J Physiol Endocrinol Metab*, 284:E241–E258, 2003.

[12] Geraldine Clough, Andrew Chipperfield, Christopher Byrne, Frits de Mul, and Rodney Gush. Evaluation of a new high power, wide separation laser doppler probe: Potential measurement of deeper tissue blood flow. *Microvascular Research*, 78:155–161, 2009.

[13] Jean-Luc Cracowski, C.T. Minson, M. Salvat-Melis, and J.R. Halliwill. Methodological issues in the assessment of skin microvascular endothelial function in humans. *Trends in Pharmacological Sciences*, 27(9):503–508, 2006.

[14] C.H.A de Haan, F.M.H. van Dielen, A.J.H.M. Houben, P.W. de Leeuw, F.C. Huvers, J.G.R. De Mey, and B.H.R Wolffenbuttel. Peripheral blood flow and noradrenaline responsiveness: the effect of physiological hyperinsulinemia. *Cardiovascular Research*, 34:192–198, 1997.

[15] RT de Jongh, EH Serne, RG IJzerman, HT Jorstad, and CDA Stehouwer. Impaired local microvascular vasodilatory effects of insulin and reduced skin microvascular vasomotion in obese women. *Microvascular Research*, 75:256–262, 2008.

[16] Frits F.M. de Mul, Fernando Morales, Andries J. Smit, and Reindert Graaff. A model for post-occlusive reactive hyperemia as measured with laser-dopper perfusion monitoring. *IEEE Transactions on Biomedical Engineering*, 52(2):184–190, 2005.

[17] R A DeFronzo and E Ferrannini. Insulin resistance. a multifaceted syndrome responsible for niddm, obesity, hypertension, dyslipidemia, and atherosclerotic cardiovascular disease. *Diabetes Care*, 14:173–194, 1991.

[18] R.H. Eckel, S.M. Grundy, and P.Z. Zimmet. The metabolic syndrome. *Lancet*, 365:1415–1427, 2005.

[19] Michael T. Johnstone et al. Impaired endothelium-dependent vasodilation in patients with insulin-dependent diabetes mellitus. *Circulation*, 88(6):2510–2516, 1993.

[20] Earl S. Ford, Wayne H. Giles, and William H. Dietz. Prevalence of the metabolic syndrome among us adults - findings from the third national health and nutrition examination survey. *JAMA*, 287(3):356–359, 2002.

[21] JC. Frisbee. Obesity, insulin resistance, and microvessel density. *Microcirculation*, 14:289–298, 2007.

[22] Y.C. Fung. *Biomechanics - Mechanical Properties of Living Tissues (2nd ed.)*. Springer, 1993.

[23] Y.C. Fung. *Biomechanics - Circulation*. Springer, 1997.

[24] R.F. Furchgott and J.V. Zawadzki. The obligatory role of endothelial cells in the relaxation of arterial smooth muscle by acetylcholine. *Nature*, 288:373–376, 1980.

[25] P. Goupillaud, A. Grossman, and J. Morlet. Cycle-octave and related transforms in seismic signal anallysis. *Geoexploration*, 23:85–102, 1984.

[26] KL Hardie, JS Silberberg, S Kinlay, PJ Fletcher, DB Hardy, and J Wlodarczyk. Reproducibility of brachial ultrasonography and flow-mediated dilatation (fmd) for assessing endothelial function. *Aust NZ J Med*, 27:649–652, 1997.

[27] B.L. Hodnett and R.L. Hester. Regulation of muscle blood flow in obesity. *Microcirculation*, 14:273–288, 2007.

[28] L.J. Ignarro, G.M. Buga, K.S. Wood, R.E. Byrns, and G. Chaudhuri. Endothelium-derived relaxing factor produced and release from artery and vein is nitric oxide. *Proceedings of National Academy of Sciences*, 84:9265–9296, 1987.

[29] William B. Kannel and Daniel L. McGee. Diabetes and cardiovascular disease. *JAMA*, 241:2035–2038, 1979.

[30] T. Kijewski and A. Kareem. Wavelet transforms for system identification in civil engineering. *Computer-aided civil and infrastructure engineering*, 18:339–355, 2003.

[31] Per Kvandal, Svein Aslak Landsverk, Alan Bernjak, Aneta Stefanovska, Hebe Desiree Kvernmo, and Knut Arvid Kirkeboen. Low-frequency oscillations of the laser doppler perfusion signal in human skin. *Microvascular Research*, 72:120–127, 2006.

[32] Hebe Desiree Kvernmo, Aneta Stefanovska, and Maja Bracic. Spectral analysis of the laser doppler perfusion signal in human skin before and after exercise. *Microvascular Research*, 56:173–182, 1998.

[33] J.R. Levick. *An Introduction to Cardiovascular Physiology, 4th edition.* ARNOLD, 2001.

[34] KJ Mather, B Mirzamohammadi, Amale Ltelf, HO Steinberg, and AD Baron. Endothelin contributes to basal vascular tone and endothelial dysfunction in human obesity and type 2 diabetes. *Diabetes*, 51(12):3517–3523, 2002.

[35] M.F. Meyer, D. Lieps, H. Schatz, and M. Pfohl. Impaired flow-mediated vasodilation in type 2 diabetes: lack of relation of microvascular dysfunction. *Proceedings of the IEEE*, 84(4):626–638, 1996.

[36] Fernando Morales. *Improving the clinical applicability of laser Doppler perfusion monitoring.* PhD thesis, Rijkuniversiteit Groningen, 2005.

[37] Robert B. Northrop. *Noninvasive Instrumentation and Measurement in Medical Diagnosis.* CRC Press, 2002.

[38] H. Nyquist. Certain topics in telegraph transmission theory - reprinted. *Proceedings of the IEEE*, 90(2):280–305, 2002.

[39] Alan V. Oppenheim and Alan S. Willsky. *Signals and Systems.* Prentice Hall, 1997.

[40] J.H. Pinkney, C.D.A. Stehouwer, S.W. Coppack, and J.S. Yudkin. Endothelial dysfunction: Cause of the insulin resistance syndrome. *Diabetes*, 46:S9–S13, 1997.

[41] Jordan S. Pober and William C. Sessa. Evolving functions of endothelial cells in inflammation. *Nature Reviews Immunology*, 7:803–815, 2007.

[42] Shie Qian. *Introduction to Time-Frequency and Wavelet Transforms.* Prentice Hall, 2002.

[43] M. Rossi, A. Carpi, F. Galetta, F. Franzoni, and G. Santoro. The investigation of skin blood flowmotion: a new approach to study the microcirculatory impairment in vascular diseases? *Biomedicine & Pharmacotherapy*, 60:437–442, 2006.

[44] John L. Semmlow. *Biosignal and Biomedical Image Processing.* Dekker Media, 2004.

[45] E.H. Serne, R.O.B. Gans, J.C. ter Maaten, Geert-Jan Tangelder, Ab J.M. Donker, and C.D.A. Stehouwer. Impaired skin capillary recruitment in essential hypertension is caused by both functional and structural capillary rarefaction. *Hypertension*, 38:238–242, 2001.

[46] Claude E. Shannon. Communication in the presence of noise - reprinted. *Proceedings of the IEEE*, 96(2):447–457, 1998.

[47] Dee Unglaub Silverthorn. *Human Physiology*. Prentice Hall, 2007.

[48] Julius O. Smith. Spectral audio signal processing, March 2010.

[49] Samuel D. Stearns. *Digital Signal Processing with Examples in MATLAB*. CRC Press, 2003.

[50] Aneta Stefanovska. Physics of the human cardiovascular system. *Contemporary Physics*, 40(1):31–55, 1999.

[51] Aneta Stefanovska, Maja Bracic, and Hebe Desiree Kvernmo. Wavelet analysis of oscillations in the peripheral blood circulation measured by laser doppler technique. *IEEE Transactions on Biomedical Engineering*, 46(10):1230–1239, 1999.

[52] M.D. Stern. In vivo evaluation of microcirculation by coherent light scattering. *Nature*, 254:56–58, 1975.

[53] T Teland, EG Salerud, GE Nilsson, and PA Oberg. Spatial and temporal variations in human skin blood flow. *Int J Microcirc Clin Exp*, 2:81–90, 1983.

[54] Brani Vidakovic. *Statistical Modeling by Wavelets*. Wiley, 1999.

[55] M.B. Wilk and S.S. Shapiro. The joint assessment of normality of several independent samples. *Technometrics*, 10(4):825–839, 1968.

[56] IB Wilkinson, SA Fuchs, IM Jansen, JC Spratt, GD Murray, JR Cockcroft, and DJ Webb. Reproducibility of pulse wave velocity and augmentation index measured by pulse wave analysis. *Journal of Hypertension*, 16:2079–2084, 1998.

[57] M. Yanagisawa, H. Kurihara, S. Kimura, Y. Tomobe, M. Kobayashi, Y. Mitsui, Y. Yazaki, K. Goto, and T. Masaki. A novel potent vasoconstrictor peptide produced by vascular endothelial cells. *Nature*, 332:411–415, 1988.